Check for updates

Small

NANO · MICRO small
www.small-journal.com

RESEARCH ARTICLE OPEN ACCESS

Eutectic Mixtures of Inorganic and Organic Adamantane-Type Compounds With Strongly Nonlinear Optical Properties

Irán Rojas León[1] | Jan Christmann[1] | Saravanan Gowrisankar[2,3] | Sebastian Schwan[3,4] | Anton S. Nizovtsev[3,4] | Ferdinand Ziese[3,5] | Jürgen Belz[6,7] | Johannes Haust[6,7] | Jihed Ayari[8] | Kerstin Volz[6,7] | Nils W. Rosemann[9] | Simone Sanna[3,5] | Doreen Mollenhauer[3,4,10,11,12] | Klaus Jurkschat[8] | Peter R. Schreiner[2,3] | Stefanie Dehnen[1]

[1]Institute of Nanotechnology, Karlsruhe Institute of Technology, Karlsruhe, Germany | [2]Institute of Organic Chemistry, Justus-Liebig University, Giessen, Germany | [3]Center for Materials Research (ZfM), Justus-Liebig University Giessen, Giessen, Germany | [4]Institute of Physical Chemistry, Justus-Liebig University Giessen, Giessen, Germany | [5]Institute of Theoretical Physics, Justus-Liebig University Giessen, Giessen, Germany | [6]Philipps-Universität Marburg, Department of Physics, Functional Materials, Marburg, Germany | [7]Philipps-Universität Marburg, Marburg Center for Quantum Materials and Sustainable Technologies (mar.quest), Marburg, Germany | [8]Technische Universität Dortmund, Fakultät für Chemie und Chemische Biologie, Dortmund, Germany | [9]Light Technology Institute, Karlsruhe Institute of Technology, Karlsruhe, Germany | [10]Institute for Technical and Environmental Chemistry, Friedrich Schiller University Jena, Jena, Germany | [11]Helmholtz Institute for Polymers in Energy Applications Jena (HIPOLE Jena), Jena, Germany | [12]Helmholtz-Zentrum Berlin für Materialien Und Energie GmbH (HZB), Berlin, Germany

Correspondence: Klaus Jurkschat (klaus.jurkschat@tu-dortmund.de) | Peter R. Schreiner (prs@uni-giessen.de) | Stefanie Dehnen (stefanie.dehnen@kit.edu)

Received: 11 July 2026 | **Revised:** 11 July 2026 | **Accepted:** 28 August 2026

Keywords: adamantane | amorphous solid | chemistry | eutectic system | inorganic chemistry | material properties | materials science | nonlinear optics

ABSTRACT

We report a new concept to lower the melting temperature (T_m) of inorganic-organic hybrid adamantane-based cluster compounds by forming unprecedented eutectic cluster mixtures with organic adamantane derivatives. Blending of clusters of the type [(*p*-$MeC_6H_4Si(CH_2SnPhE)_3$] (E = S, Se, Te) with (3-F-4-Me-C_6H_3)$_3$Ad, (3-F-4-Me-Ph)$_4$Ad, and (4-MeO-C_6H_4)$_4$Ad was achieved by mechanical mixing and led to decreased T_m while retaining the components' chemical identity. Such adamantane-type compounds are known to exhibit strongly non-linear optical properties: upon irradiation with a continuous wave (CW) laser diode, they respond either by second-harmonic generation (SHG), if being crystalline, or by white-light generation (WLG) with corresponding broadband emission, if being intrinsically amorphous or transformed into a glassy state. Herein, we show that this feature is preserved in the eutectic mixtures, hence, we can report superior properties of these cluster-based materials that combine favorable nonlinear optical behavior with lowered T_m, which facilitates their processing for future use.

1 | Introduction

Physical and optical properties (second harmonic generation, SHG, or white-light generation, WLG) [1–13] of crystalline or amorphous solids have been investigated with increasing activity in recent years due to potential applications in everyday devices [3–7]. Inorganic and organic hybrid compounds are an emerging new class of functional materials due to their variability in structural types, ease of synthesis, and tunable band gaps across the whole visible spectrum [14]. In general, most inorganic and organic hybrid compounds are synthesized by multistep and costly chemical reactions to study nonlinear optical

This is an open access article under the terms of the Creative Commons Attribution License, which permits use, distribution and reproduction in any medium, provided the original work is properly cited.
© 2026 The Author(s). *Small* published by Wiley-VCH GmbH

properties [15–17]. Very recently, nonlinear optical (NLO) properties were reported for deep eutectic solvent mixtures, like choline chloride [18], tetramethylammonium chloride, and 1-butyl-3-methylimidazolium [19, 20]. Adamantane derivatives [21] as well as adamantane-type clusters with the general formula $[(RT)_4E_6]$ (R = organic substituent, T = C, Si, Ge, Sn, and E = S, Se, Te or CH_2), in their amorphous state, exhibit highly directional white-light emission when being excited by infrared light from an inexpensive continuous wave (CW) laser diode [2, 22–26]. The extremely low degree of periodic order of the molecules in the amorphous powders seems to be one of the necessary preconditions for WLG [22, 27–36]. In contrast, crystalline or sufficiently ordered samples of such molecular materials do not show WLG, but exhibit intense SHG instead [23, 37]. The origin of these phenomena is currently under intense investigation. In this context, also the generation of glassy materials from crystalline adamantane–type clusters $[(C_6H_4Si(CH_2SnPhE)_3]$ (E = S, Se, Te) has only recently been reported by some of the authors [25].

Generally, crystalline solids with glass transitions above the melting temperature have shown remarkable dynamic and thermodynamic behavior in glasses and supercooled liquids [38, 39]. The glass transition temperature (T_g) is a critical parameter for the physical properties of materials, such as the shear viscosity $\eta(T,x)$, crucial for all stages of industrial glass production [40, 41]. Accurate knowledge of the dependence of $\eta(T,x)$ from T_g and the composition (x) is of utmost importance. While glasses from purely organic or purely inorganic adamantane-like molecules have not been reported yet, the formation of glasses derived from hybrid organic–inorganic adamantane-type clusters recently emerged [42, 43]. For binary and multicomponent systems, the dependence of T_g on the composition is a key parameter for exploring the structural relaxation dynamics in glass-forming mixtures [44–46].

Despite the impressive development of white-light emitting materials using purely organic or Sn/S- and Si/S-based cluster materials, respectively, yet another degree of freedom for innovative emissive systems would be provided by a corresponding blend of such compounds. We were thus wondering whether it is possible to retain the beneficial optical properties while lowering the melting temperature by the formation of a eutectic mixture. To explore this possibility, we employed a simple melting procedure to mix purely organic adamantane (Ad) derivatives with inorganic–organic hybrid adamantane-type clusters. Herein, we report success by the unprecedented approach to corresponding eutectic cluster mixtures with the desired lower melting temperatures. For this, we synthesized new organotin chalcogenide clusters $[(p\text{-}MeC_6H_4Si(CH_2SnPhE)_3]$ (E = S, Se, Te), studied their ability to mix with compounds $(3\text{-F-4-Me-}C_6H_3)_3Ad$, $(3\text{-F-4-Me-Ph})_4Ad$, and $(4\text{-MeO-}C_6H_4)_4Ad$, and explored the NLO response of the pure compounds as well as the mixtures upon irradiation with laser light, both experimentally and by computations.

2 | Results

2.1 | Syntheses of Adamantane-Type Compounds

In analogy to the procedure reported in the literature [47, 48], and as illustrated in Scheme 1, the reaction of $p\text{-}MeC_6H_4Si(CH_2Cl)_3$ (**1**) with Ph_3SnNa in THF gave p-tolyl-tris(triphenylstannylmethyl)silane $p\text{-}MeC_6H_4Si(CH_2SnPh_3)_3$ (**2**). Its treatment with HCl provided the hexachlorido-substituted organotin derivative $p\text{-}MeC_6H_4Si(CH_2SnCl_2Ph)_3$ (**3**). Both **2** and **3** are colorless solid materials that show good solubility in organic solvents such as CH_2Cl_2, CH_3Cl, THF, toluene, and benzene.

By reaction in toluene with bis(trimethylsilyl) chalcogenides $(Me_3Si)_2E$ (E = S, Se, Te), hereafter referred to as $(TMS)_2E$ (see Scheme 1) the organotin chloride **3** was converted in good yields to the corresponding organotin chalcogenides $[(p\text{-}MeC_6H_4Si(CH_2SnPhE)_3]$ (**4**, E = S; **5**, E = Se, **6**, E = Te). The products were characterized by elemental analysis, by ^{1}H, ^{13}C, ^{29}Si, ^{77}Se, ^{125}Te, and ^{119}Sn nuclear magnetic resonance (NMR) spectroscopy (Figures S1–S3, S5–S7, S9, S11–S14, S18–S22, and S26–S30), by infrared (IR) spectroscopy (Figures S4, S8, S10, S17, and S25), electrospray ionization mass spectrometry (ESI MS; Figures S15, S23, and S31), by thermogravimetric analysis (TGA; Figures S16, S24, and S32), and by powder-X-ray diffraction (Figure S33). Details about the analytic methods are provided in the Supporting Information for details). Single crystals of compounds **4–6** suitable for single-crystal X-ray diffraction analysis were obtained from their solutions in hexane.

The synthesis of $(3\text{-F-4-Me-}C_6H_3)_3Ad$ (**7**), $(3\text{-F-4-Me-Ph})_4Ad$ (**8**), and $(4\text{-MeO-}C_6H_4)_4Ad$ (**9**) has been reported using various of synthetic methods [49–54]. We followed the most typical synthetic approach as shown in Scheme 1.

The synthetic routes to the adamantane-type cluster compounds **4 – 6** as well as the all-organic adamantane derivatives **7 – 9** are outlined in Scheme 1.

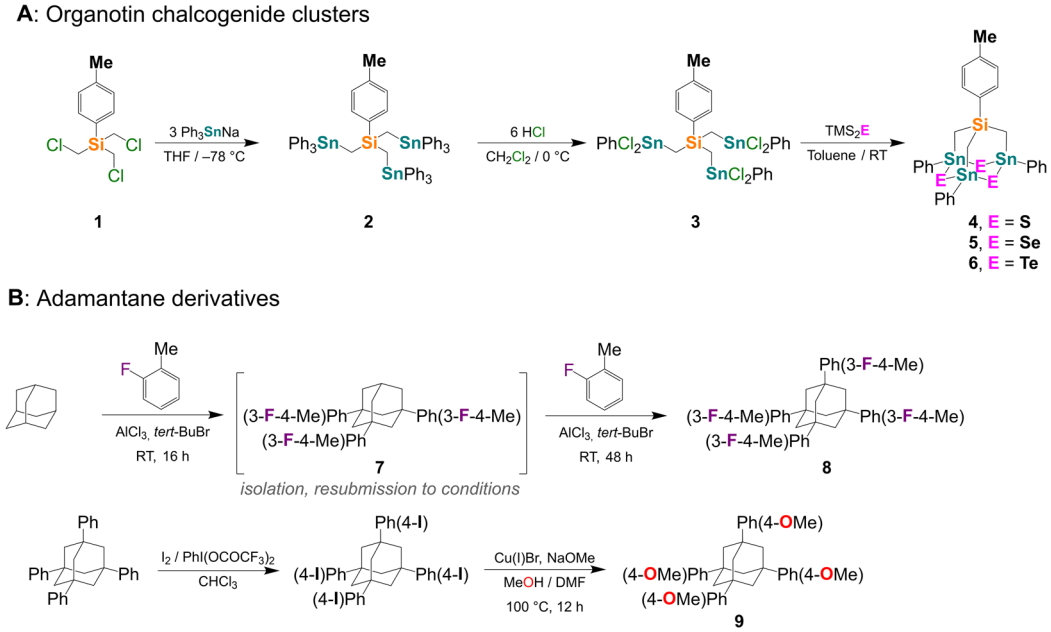
2.2 | Solid-State Structures of Hybrid Inorganic–Organic Adamantane Type-Clusters

Compounds **4–6** are isomorphous and crystallize in the monoclinic space group *P*21/*c*. Figure 1 shows the molecular and crystal structures of the heteronuclear adamantane-type clusters **4–6**; Table 1 contains selected interatomic distances and angles. Crystallographic and refinement details are given in Table S1.

The Sn–CH_2 [2.121(9)–2.143(3) Å] and Sn–E distances [**4**, 2.5223(8)–2.5423(8); **5**, 2.5223(8)–2.5423(8); **6**, 2.7122(3)–2.7373(3) Å] are as expected and thus similar to the corresponding distances reported previously for the PhSi-containing analogues [25]. In line with the well-known increasing s-character of the lone electron pairs at the chalcogen atoms with increasing atomic number, and thus the dominance of *p*-orbital contributions to bonding [55–57], the Sn–E–Sn angles decrease to approach the 90° value as going from **4** (E = S; 97.57(8)–98.33(10)°) via **5** (E = Se; 94.15(2)–94.97(2)°) to **6** (E = Te; 89.954(10)–91.362(10)°).

A remarkable feature in the crystal structures is the formation of 'pairs' via intermolecular E→π interactions between the chalcogenides and phenyl groups with element-to-centroid C(41)···C(46) distances of 4.02 (**4**), 3.84 (**5**), and 3.80 Å (**6**). The different distances result from the different van der Waals radii of S (1.80 Å), Se (1.90 Å), and Te (2.00 Å) [58, 59].

16136829, 0, Downloaded from https://onlinelibrary.wiley.com/doi/10.1002/smll.75964 by Karlsruher Institut Fur Technologie, Wiley Online Library on [03/11/2026]. See the Terms and Conditions (https://onlinelibrary.wiley.com/terms-and-conditions) on Wiley Online Library for rules of use; OA articles are governed by the applicable Creative Commons License



SCHEME 1 | Synthetic routes for the preparation of the compounds discussed in this work. A: Synthesis of the adamantane-type organotin chalcogenide clusters **4 – 6**. B: Synthesis of adamantane derivatives **7 – 9**.

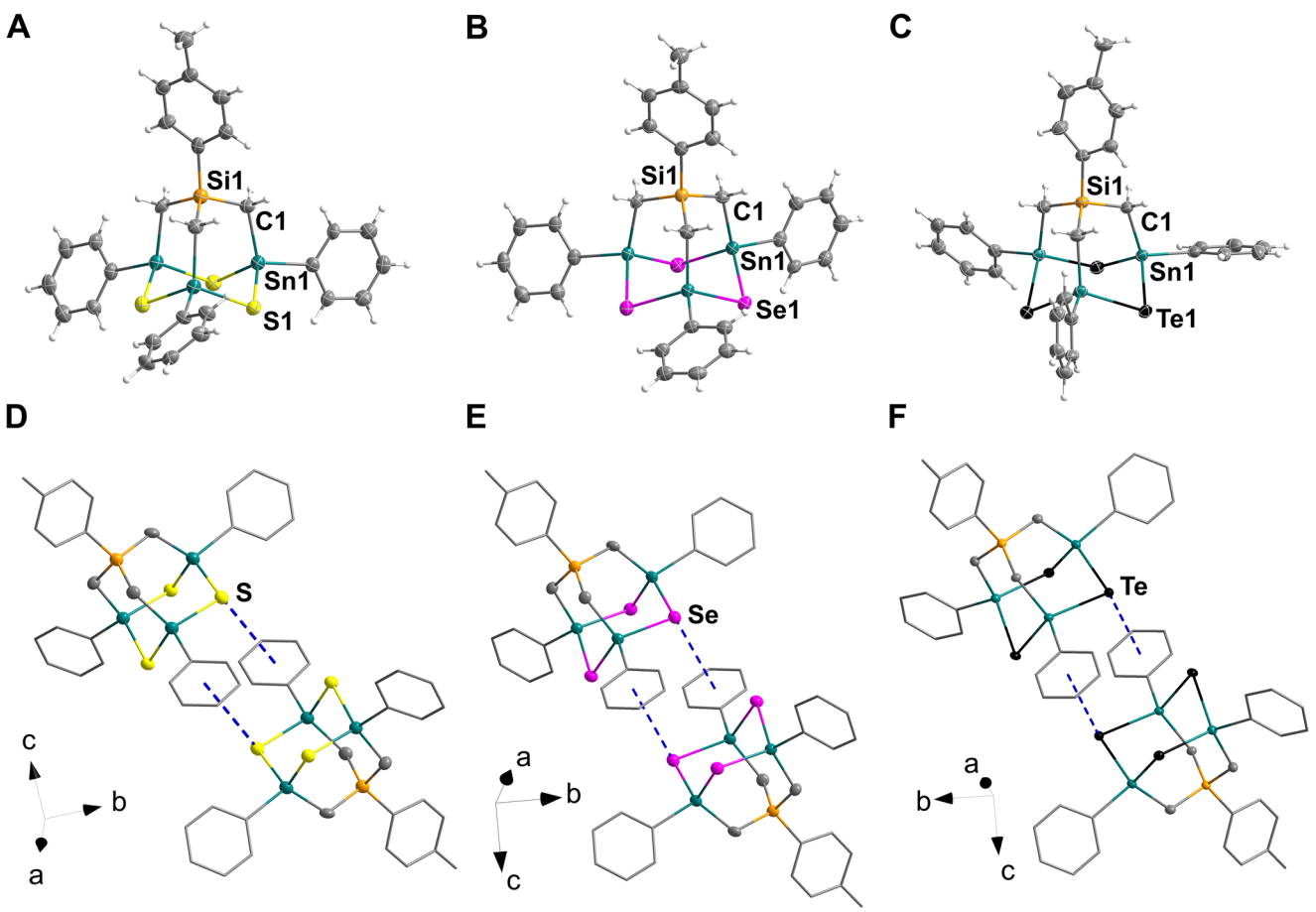


FIGURE 1 | A–C: Molecular structures of the heteronuclear adamantane-type clusters **4** (A), **5** (B), and **6** (C). D–F: Cut-out of the crystal structures of **4** (D), **5** (E), and **6** (F), highlighting the intermolecular interactions leading to 'pair' formation. Hydrogen atoms are omitted in panels D–F for clarity. Thermal ellipsoids are drawn at the 30% probability level. Supplementary crystallographic figures are provided in Figure S34.

16136829, 0, Downloaded from https://onlinelibrary.wiley.com/doi/10.1002/smll.75964 by Karlsruher Institut Fur Technologie, Wiley Online Library on [03/11/2026]. See the Terms and Conditions (https://onlinelibrary.wiley.com/terms-and-conditions) on Wiley Online Library for rules of use; OA articles are governed by the applicable Creative Commons License

TABLE 1 | Selected interatomic distances (Å), and angles (°) for **4**, **5**, and **6**.

Compound	4	5	6
E	S	Se	Te
Sn−CH_2	2.121(9)–2.128(9)	2.129(6)–2.141(6)	2.139(3)–2.143(3)
Sn−E	2.407(3)–2.417(3)	2.5223(8)–2.5423(8)	2.7122(3)–2.7373(3)
Si−CH_2	1.841(10)–1.874(9)	1.859(7)–1.860(7)	1.857(4)–1.864(4)
Si−CH_2−Sn	117.4(5)–119.9(4)	117.8(3)–121.0(3)	119.48(18)–122.09(17)
CH_2−Sn−E	108.3(3)–112.3(3)	108.55(17)–112.94(18)	109.16(9)–113.01(11)
E−Sn−E	106.61(9)–110.61(9)	107.96(3)–112.85(3)	109.512(11)–114.14(11)
Sn−E−Sn	97.57(8)–98.33(10)	94.15(2)–94.97(2)	89.954(10)–91.362(10)

The identity of **4–6** is retained in solution, as is apparent from the ^{119}Sn NMR spectra, showing singlet resonances at δ 101 ppm [^2J(^{119}Sn-C-^{117}Sn) = 90 Hz] (**4**), δ 5 ppm [^2J(^{119}Sn-C-^{117}Sn) = 113 Hz, ^1J(^{119}Sn-^{77}Se) = 614 Hz] (**5**), and δ –246 ppm [^2J(^{119}Sn-C-^{117}Sn) = 105 Hz, ^1J(^{119}Sn-^{125}Te) = 1533 Hz] (**6**), respectively. The chemical shifts are similar to the data reported for related six-membered diorganotin chalcogenide rings $(RSnS)_3$, $(PhRSnSe)_3$, and $(PhRSnTe)_3$ [60, 61]. A ^{77}Se NMR spectrum of **5** exhibits a single resonance at δ –349 ppm [^1J(^{77}Se-$^{117/119}$Sn) = 586/613 Hz]. The same holds for a ^{125}Te NMR spectrum of **6**, showing a resonance at δ –864 ppm [^1J(^{125}Te-$^{117/119}$Sn) = 3069/2929 Hz] [62–64]. Given the (idealized) C_{3v}-symmetric structures of **4–6**, their ^{1}H and ^{13}C NMR spectra are rather simple and show the expected resonances for the CH_2, phenyl, and *p*-tolyl moieties (see Supporting Information).

The ESI mass spectra of **4–6** reveal mass clusters centered at m/z = 866.8068 (**4**, assigned to $[M+Na]^+$), m/z = 1008.6434 (**5**, assigned to $[M+Na]^+$), and m/z = 1166.5863 (**6**, assigned to $[M+Cl]^+$). The experimental spectra match the calculated ones (Figures S15, S23, and S31).

2.3 | Formation of Glassy Materials from Inorganic–Organic Hybrid Adamantane-Type Clusters

In order to produce amorphous glasses from the crystalline adamantane-type compounds **4–6**, they were exposed to the melting temperatures (195–202°C for **4**, 201–206°C for **5**, and 205–210°C for **6**) and subsequently shock-cooled. The resulting glassy materials were analyzed by powder X-ray diffraction (PXRD), which revealed the formation of amorphous solids (for comparison with the crystalline phases see Figure 2A,B; Figures S35A,B and S36A,B). ^{1}H NMR spectra of the redissolved crystalline and glassy materials indicate that both consist of the same molecular species (Figure 2C; Figures S35C and S36C). The melting process was monitored by differential scanning calorimetry (DSC) (Figure 2D; Figures S35D and S36D), with the occurrence of an endothermic feature allowing to determine the temperature range. EDX analyses were performed to identify the heavy elements and to determine their ratio (Figure 2E; Figures S35E and S36E). The experimental values show good agreement with the calculated ones. Thermogravimetric analyses (TGA) revealed mass losses at 405°C (**4**), 382°C (**5**), and 315°C (**6**) (Figure 2F; Figures S35F and S36F). In addition, scanning electron microscopy (SEM) images support the materials' physical transformation from a crystalline powder (Figure 2; Figures S35 and S36: insets I and II) to glasses (Figure 2; Figures S35 and S36: insets III and IV).

2.4 | Mixtures of Organic and Inorganic–Organic Hybrid Cluster Materials

With this information at hand, we explored the materials properties upon physical blending with organic analogues. Based on the structural similarities of the adamantane-type organotin chalcogenide cluster **4–6** and the all-organic adamantane derivatives **7–9**, as well as the melting of the latter at moderate temperatures [T_m: 214–219°C (**7**), 258–260°C (**8**), 250–253°C (**9**)] [54], we expected to see the formation of unprecedented eutectic mixtures of adamantane-type clusters and adamantane derivatives. We set out to determine whether mixtures of both would give hybrid glassy materials and whether both components keep their molecular identity within these materials. The equimolar (1:1) mixtures of the two cluster types are illustrated in Scheme 2, using compound **4** as an example on the inorganic-organic side, with **7**, **8**, or **9** added as organic counterpart.

Monitoring of the persisting identity of the clusters within the mixtures while significantly changing the crystallinity of the composites is documented in Figure 3 for the **4/7**, **4/8**, and **4/9** mixtures, respectively; these show very similar behaviors. The 1:1 mixtures were obtained by co-melting compound **4** with either **7**, **8**, or **9**. We used the melt-quenching technique in melting temperature determination tubes (80 × 1.3 mm), filled with 5 mg of a preformed mixture of crystalline powders. Starting from the crystalline samples according to powder X-ray diffraction (PXRD; Figure 3A,D,G for **4/7**, **4/8**, and **4/9**, respectively), the systems were left under reduced pressure (1×10^{-3} mbar) for 30 min, and the capillaries sealed thereupon. Then, the solids were melted using a temperature ramp of 1°C s^{-1}. As soon as the samples **4/7**, **4/8**, and **4/9** reached their corresponding melting temperatures (164–172°C, 194–206°C, and 175–183°C, respectively), a phase change occurred. The capillaries were removed from the melting device and cooled to room temperature. PXRD studies confirmed the resulting glassy materials to be highly amorphous (Figure 3B,E,H for **4/7**, **4/8**, and **4/9**, respectively). ^{1}H NMR experiments were carried out before and after glass

16136829, 0, Downloaded from https://onlinelibrary.wiley.com/doi/10.1002/smll.75964 by Karlsruher Institut Fur Technologie, Wiley Online Library on [03/11/2026]. See the Terms and Conditions (https://onlinelibrary.wiley.com/terms-and-conditions) on Wiley Online Library for rules of use; OA articles are governed by the applicable Creative Commons License

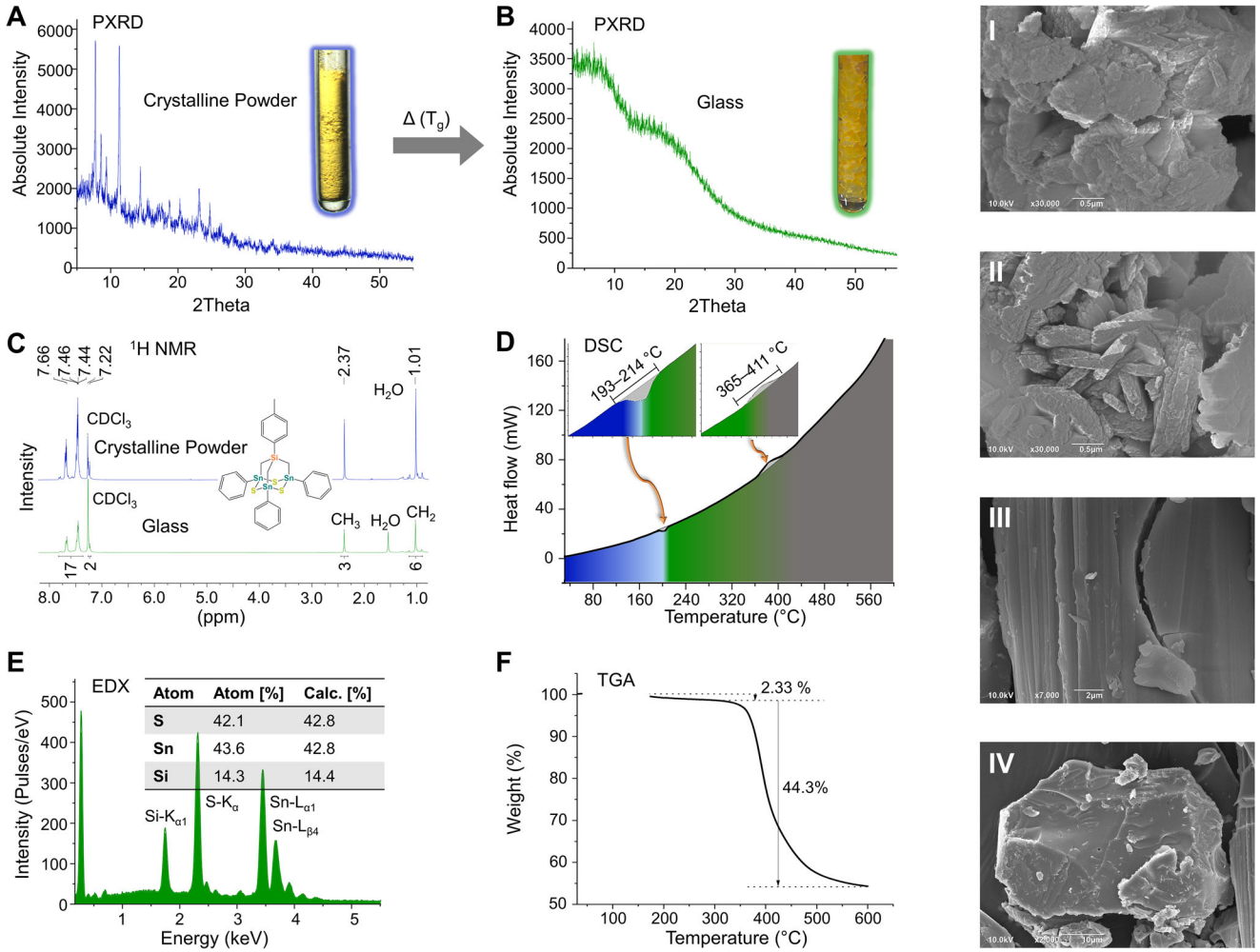
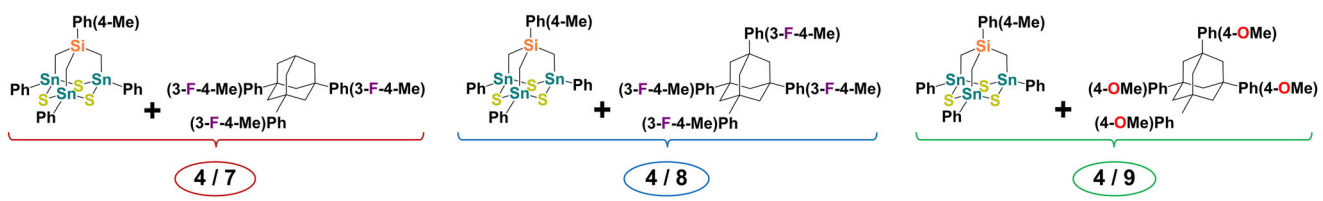


FIGURE 2 | Properties of the glassy material **4** (as an example for similarly behaving compounds **4**–**6**) formed by thermal treatment of the heteronuclear adamantane-type organotin chalcogenides. A: PXRD diagram and photograph of the crystalline material before melting. B: PXRD diagram and photograph of the glassy material upon cooling down the capillary. C: ^{1}H NMR spectra of both samples dissolved in $CDCl_3$, proving their chemical identity. D: Differential scanning calorimetry (DSC) curve indicating the endothermic melting step at 193–214°C and the exothermic decomposition around 365–411°C. E: Energy-dispersive X-ray (EDX) spectrum confirming the desired S:Sn:Si ratio of the quaternary adamantane-type cluster compounds in the cluster-glass material. D: Thermal gravimetric analysis (TGA) curve indicating the decomposition temperature T_d around 400°C. Insets I, II: Scanning electron microscopy (SEM) images of the as-prepared crystalline powder (× 30 000). Insets III, IV: SEM images of the glassy surfaces after the melting process of the material (× 7000 and × 2000).



SCHEME 2 | Schematic drawing of the adamantane-type clusters and all- adamantane derivatives used for the preparation of eutectic cluster mixtures.

formation of the mixtures, which confirmed that the compounds did not decompose during the transition (Figure 3C,F,I). SEM images confirm the physical transformation of the materials, from micro-crystalline solids (Figure 3J,L and 3N) to hybrid glassy materials with smooth surfaces (Figure 3K,M,O). The findings are supported by TEM studies. The TEM images and corresponding diffraction patterns of the four samples (**4**, **4/7**, **4/8**, and **4/9**, Figure S38) clearly indicate a decrease in crystallinity upon transformation into the glassy state.

To study the melting process in greater detail, TGA and DSC analyses were performed upon drying the as-prepared crystalline

16136829, 0, Downloaded from https://onlinelibrary.wiley.com/doi/10.1002/smll.75964 by Karlsruher Institut Fur Technologie, Wiley Online Library on [03/11/2026]. See the Terms and Conditions (https://onlinelibrary.wiley.com/terms-and-conditions) on Wiley Online Library for rules of use; OA articles are governed by the applicable Creative Commons License

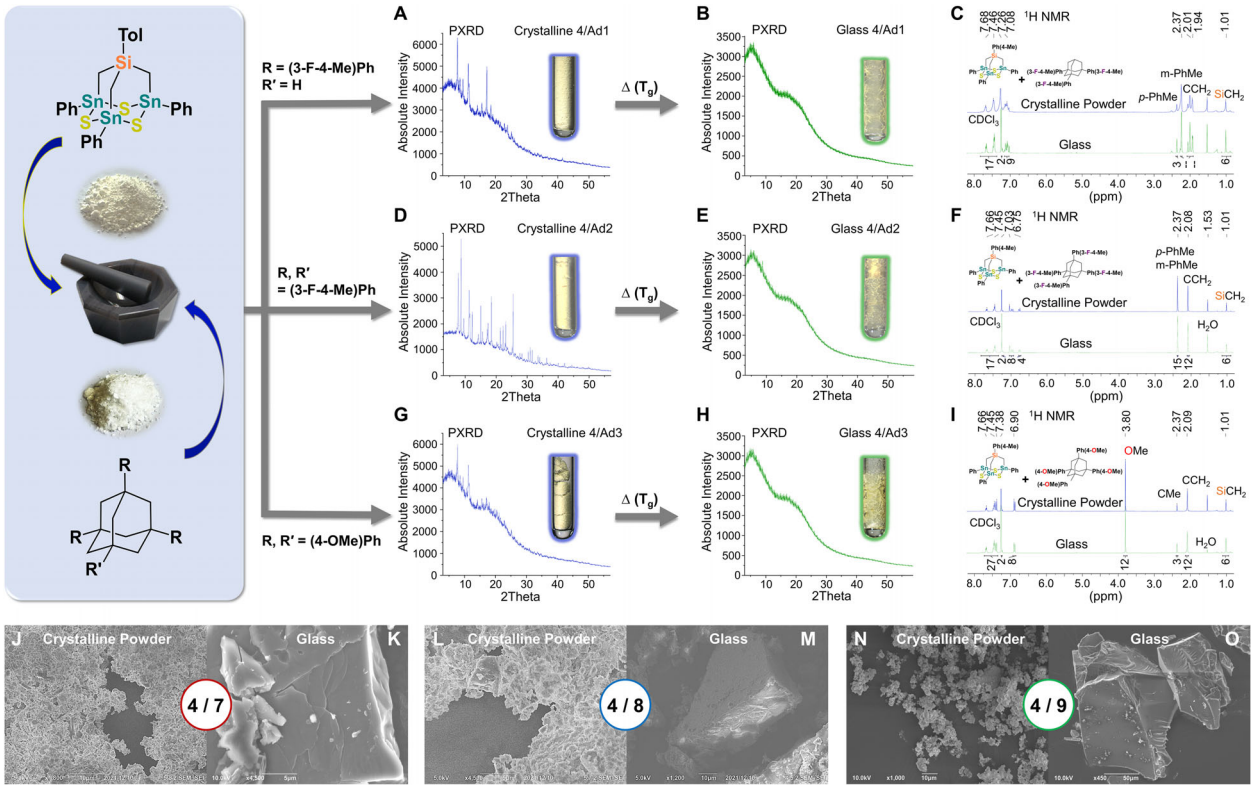


FIGURE 3 | Generation of glassy materials obtained by mixing, grinding, and melting **4** together with an organic adamantane derivative. A, D, G: PXRD diagrams and photographs of the crystalline materials **4/7**, **4/8**, and **4/9**. B, E, H: PXRD diagram and photograph of the glass-cluster upon cooling down the capillary. C, F, I: ^{1}H NMR spectra of both samples dissolved in $CDCl_3$, proving their chemical identity. N, L, J: Scanning electron microscopy (SEM) images of the as-prepared crystalline powder (× 1800; × 4500 and × 1000). O, M, K: SEM images of the glassy surfaces after thermal treatment of the crystalline powder (× 4,500; × 1200 and × 450). All measurement were performed for the mixtures **4/7**, **4/8** and **4/9** respectively.

samples to remove all solvent residues (**4/7**, **4/8** and **4/9**). In the TGA experiment, a weight loss is observed at around 400°C, indicating that the mixtures decompose (Figure 4A,B). A comparison with the corresponding behavior of pure compound **4** indicates that the decomposition behavior of the mixtures is slightly different regarding the onset of the decomposition process, its rate and the mass of the residue. In the DSC curve, a decrease in the melting temperature is clearly observed with an endothermic feature around 131–202°C and 175–191°C for the mixtures **4/7** and **4/9**, respectively (Figure 4C,E). However, for the **4/8** mixture, the endothermic feature is observed in a larger and higher-temperature range of 201–299°C (Figure 4D). We attribute this to a lower compatibility of the two clusters and thus a less homogeneous mixture, such that the molecules from the same material prefer to interact with each other and thus behave largely like the separate compounds. As demonstrated in Figure 4F–H an approximately 1:1 ratio of the two cluster types is pertained in all three samples, hence the differences in the thermochemical behavior are inherent to the nature and (mis)match within the three different cluster mixtures.

To explore whether the hybrid samples indeed behave like eutectic mixtures, we determined the melting diagram of the **4/7** mixture by DSC. While the melting temperatures of the pure compounds amount to 205°C (**4**) and 220°C (**7**), they decrease upon addition of the other component and reach a minimum value at the eutectic point, with a melting temperature of 171°C at an equimolar ratio (1:1). At this temperature and composition of the mixture, the system is invariant, that is, two solid phases and a liquid phase are in equilibrium. Above this temperature, the system gives a homogeneous liquid and below this temperature, it dissociates to give a mixture of the two solid-state compounds. The phase diagram of this system, including the confirmation of the formation of a eutectic mixture, is depicted in Figure 5.

2.5 | Comparison of the Cluster Mixtures by Computational Studies

To gain insight into the molecular interaction of these systems and their differences, computations were performed to investigate the monomer and pair structures and the binding energies of the cluster pairs.

The optimized global minimum structures of the monomeric clusters **4**, **7**, **8**, and **9** are shown in Figure 6A, those of the "homogeneous pairs" ($\mathbf{4}^{pair}$, $\mathbf{7}^{pair}$, $\mathbf{8}^{pair}$ and $\mathbf{9}^{pair}$) are depicted in Figure 6B and the optimized structures of the "mixed pairs" (**4/7**, **4/8** and **4/9**) are given in Figure 6C. All minimum pair structures show the previously observed staggered conformation [26]. While the homogeneous pair of **4** is perfectly staggered and exhibits a straight C–Si···Si–C vector, the pairs of **7** – **9** are slightly shifted and tilted against each other due to the non-symmetrical substituents. The mixed pairs show a staggered structure in each case, yet again, the molecules are not perfectly aligned due to the

16136829, 0, Downloaded from https://onlinelibrary.wiley.com/doi/10.1002/smll.75964 by Karlsruher Institut Fur Technologie, Wiley Online Library on [03/11/2026]. See the Terms and Conditions (https://onlinelibrary.wiley.com/terms-and-conditions) on Wiley Online Library for rules of use; OA articles are governed by the applicable Creative Commons License

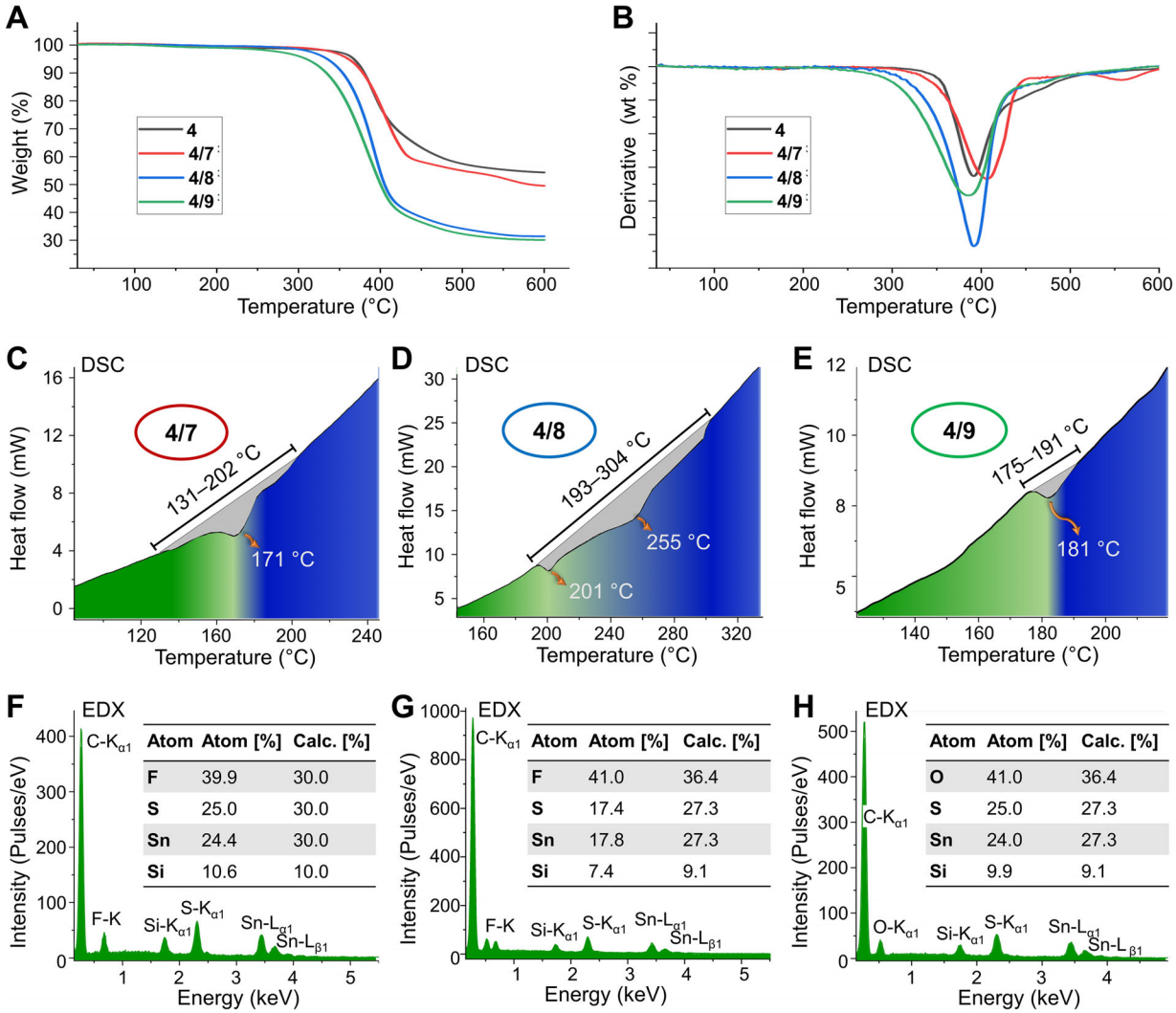


FIGURE 4 | Properties of the glassy cluster mixtures formed by thermal treatment of quaternary adamantane-type cluster compounds and organic adamantane derivatives. A, B: Thermogravimetric analysis (TGA) indicating the decomposition temperatures around 400°C. C–E: Differential scanning calorimetry (DSC) indicating an endothermic feature at temperatures of 131–202°C (**4/7**), 193–304°C (**4/8**), and 175–191°C (**4/7**), respectively. F—H: Energy-dispersive X-ray (EDX) spectra confirming the desired Se:Sn:Si composition of the mixtures **4/7**, **4/8**, and **4/9**.

unsymmetrical substituents on the adamantane derivates and the different core structures of the two molecules.

We determined the decomposition of the binding energies of the pairs as reported in earlier studies [26]. The structures were decomposed into the core and substituent moieties, and the resulting 'dangling bonds' were saturated with hydrogen atoms. From these structures, the binding energies were calculated for all seven pair structures depicted in Figure 6. The results are shown in Figure 7. The decomposition of the binding energies shows that for $\mathbf{4}^{pair}$, the core-core interaction dominates the interaction between the clusters. This seems to be typical for interactions between Sn/S-based structures and is therefore not observed for any of the other pairs. The predominance of core-core interactions also suggests that this compound prefers an amorphous solid-state habitus, in agreement with the experimental findings by PXRD, and in agreement with a relatively low melting temperature of ≈200°C. By contrast, all homogeneous adamantane pairs show very similar, dominant substituent-substituent interactions, although they differ slightly in absolute numbers. This dominant substituent-substituent interaction suggests that the organic compounds prefer a crystalline solid-state structure, which, again, is in line with their X-ray diffraction behavior and their higher melting temperatures.

The observations made for the mixed pairs are very similar to each other, with similar relative values of substituent-substituent, core-core, and core-substituent interactions (Table S2). On the other hand, all mixed pairs show weaker total interaction energies as compared to those found in the pair $\mathbf{4}^{pair}$ (ΔE_{bind} = –151 kJ mol^{-1}). Mixtures of different clusters exhibit an increase (**4/7**) or decrease (**4/8**, **4/9**) in the strength of the total interaction energies as compared to the respective homogeneous cluster pairs $\mathbf{7}^{pair}$, $\mathbf{8}^{pair}$, and $\mathbf{9}^{pair}$. Further analyses reveal a smaller gain in energy upon formation of mixed cluster pairs as compared to the energy gain found for homogeneous cluster pairs (Table 2). The results of our DFT calculations ($\Delta\Delta E_{bind}$) suggest that the thermodynamic stability of mixed pairs relative to the corresponding homogeneous cluster pairs is increased as follows **4/7**> **4/8**> **4/9**.

16136829, 0, Downloaded from https://onlinelibrary.wiley.com/doi/10.1002/smll.75964 by Karlsruher Institut Fur Technologie, Wiley Online Library on [03/11/2026]. See the Terms and Conditions (https://onlinelibrary.wiley.com/terms-and-conditions) on Wiley Online Library for rules of use; OA articles are governed by the applicable Creative Commons License

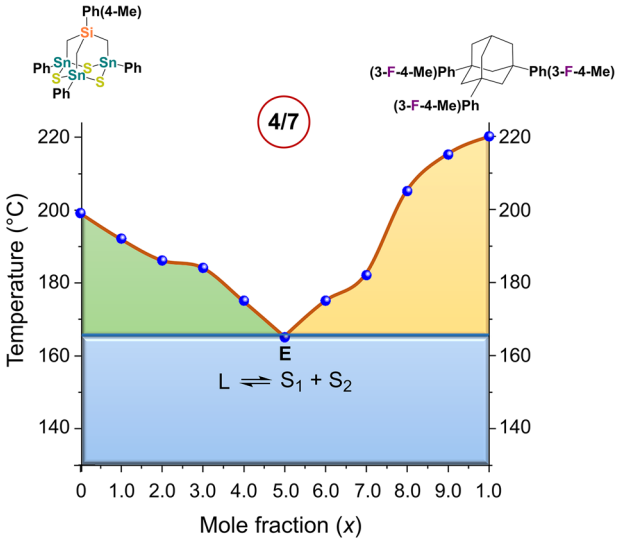


FIGURE 5 | Temperature versus mole fraction diagram of mixtures of **4** and **7**, with the mole fraction of **7** running from 0.00 to 1.00 on the horizontal axis. The melting temperatures displayed are obtained from DSC measurements.

2.6 | Investigation of the SHG Response by Computational Studies

In order to investigate how the formation of the described cluster mixtures affects the nonlinear optical response, we model the SHG response of the compounds introduced above. We remark that SHG and WLG are distinct (and often competing) optical processes, the latter involving a wealth of higher-order nonlinearities. Such processes are therefore hard to model in terms of the WLG intensity or the origin of the effect. Hence, the goal of the present investigation is to investigate the influence of the cluster mixing on the overall nonlinear optical response. To this end, we calculate the SHG response of the model compounds introduced above, and to compare it to that of their parent clusters.

Some homogeneous pairs in their minimum-energy structures feature inversion-symmetric properties that are known to eliminate almost all SHG response [65]. As inversion symmetry is impossible for mixed pair structures, those systems are promising when trying to maximize SHG activity. To investigate this relationship, we calculate the SHG response of compounds **4**–**9**, all their homogeneous pairs, $\mathbf{4}^{\text{pair}}$, $\mathbf{7}^{\text{pair}}$, $\mathbf{8}^{\text{pair}}$, and $\mathbf{9}^{\text{pair}}$, as well as the heterogeneous pairs of **4/7**, **4/8**, and **4/9** in the real-time approach within the independent particle approximation (IPA) [66–69]. Nonlinear optics calculations were performed in the real time approach within the independent particle approximation (IPA) [70]. Further details about the computational approach can be found elsewhere [71]. We compare the SHG response of the monomer to the homogeneous and heterogeneous pair structures in Figure 8 and Figure 9.

Figure 8A demonstrates that the SHG response of $\mathbf{4}^{\text{pair}}$ is quenched due to its previously described staggered configuration and concomitant inversion symmetry. This is contrasted by the comparisons in Figure 8B–D, where such a quenching does not take place due to the broken symmetries described for the organic pairs. The spectra of those pairs inherit the characteristics of their monomer counterparts, with the intensity mostly increasing up to approximately a doubling especially of the first peak, which results mostly from excitations of the highest occupied orbitals to the first few lowest unoccupied orbitals (mostly localized on the substituents).

In Figure 9, we see that the calculated SHG response of the mixed pair structures inherit characteristics of those of their monomer constituents, mostly resembling the structure **4**. Note that the intensity of the SHG response from the monomer **4** is significantly stronger than that of **7**–**9** by itself. Perhaps the most distinct property of the mixed pairs is the peak at lower energies for **4/9**. This shows possibilities to tune not only the emission intensities by creating such mixtures, but creating new "groups" of orbitals at new locations on the energy axis that were not present in the monomers and make it possible to have a high SHG intensity at much lower energies.

2.7 | Experimental Studies of the Optical Absorption and the Nonlinear Optical Response

The nonlinear optical response of all four eutectic mixtures was investigated on thin-films prepared by pulsed-laser deposition. Details on the PLD process are given in the Experimental Methods.

The thin films were placed in a vacuum chamber at a static pressure below 1×10^{-4} mbar. They were then illuminated by the output of a continuous-wave (CW) laser diode operation at 980 nm. The light emitted by the sample was collimated, relayed, and focused onto the entrance slit of a CCD-based compact spectrometer (OceanOptics HR2000). Additionally, the optical path was equipped with two bandpass filters (KG3–2 mm thickness) in order to block residual pump light. To account for the transmission profile of the filter and the other optics, the transmission of the whole system was corrected using a calibrated tungsten halogen lamp.

It is worth noting that, according to UV–visible spectra (Figure S37), optical bandgaps of the samples amount to 3.7 eV (**4**), 3.8 eV (**4/7**), or 3.9 eV (**4/8**, **4/9**). This rules out electronic transitions by a linear absorption process upon excitation with a 980 nm CW laser diode. For all four eutectic mixtures a warm-white emission was observed. For all samples an excitation density of 1100 W cm^{-2} was used. Exemplary spectra of the emission are given in Figure 10.

The observed emission spectra were converted using the 1931 CIE photopic luminosity function (for radiometric spectra see Figure S39). These photopic spectra give rise to the color impression that was observed by the human eye. The emission covers the whole visible range from ≈450 to 700 nm. As expected for the warm-white color impression, the spectra of all samples peak around 600 nm. Only minor changes of the spectra are observed depending on the illuminated sample position. We ascribe this

16136829, 0, Downloaded from https://onlinelibrary.wiley.com/doi/10.1002/smll.75964 by Karlsruher Institut Fur Technologie, Wiley Online Library on [03/11/2026]. See the Terms and Conditions (https://onlinelibrary.wiley.com/terms-and-conditions) on Wiley Online Library for rules of use; OA articles are governed by the applicable Creative Commons License

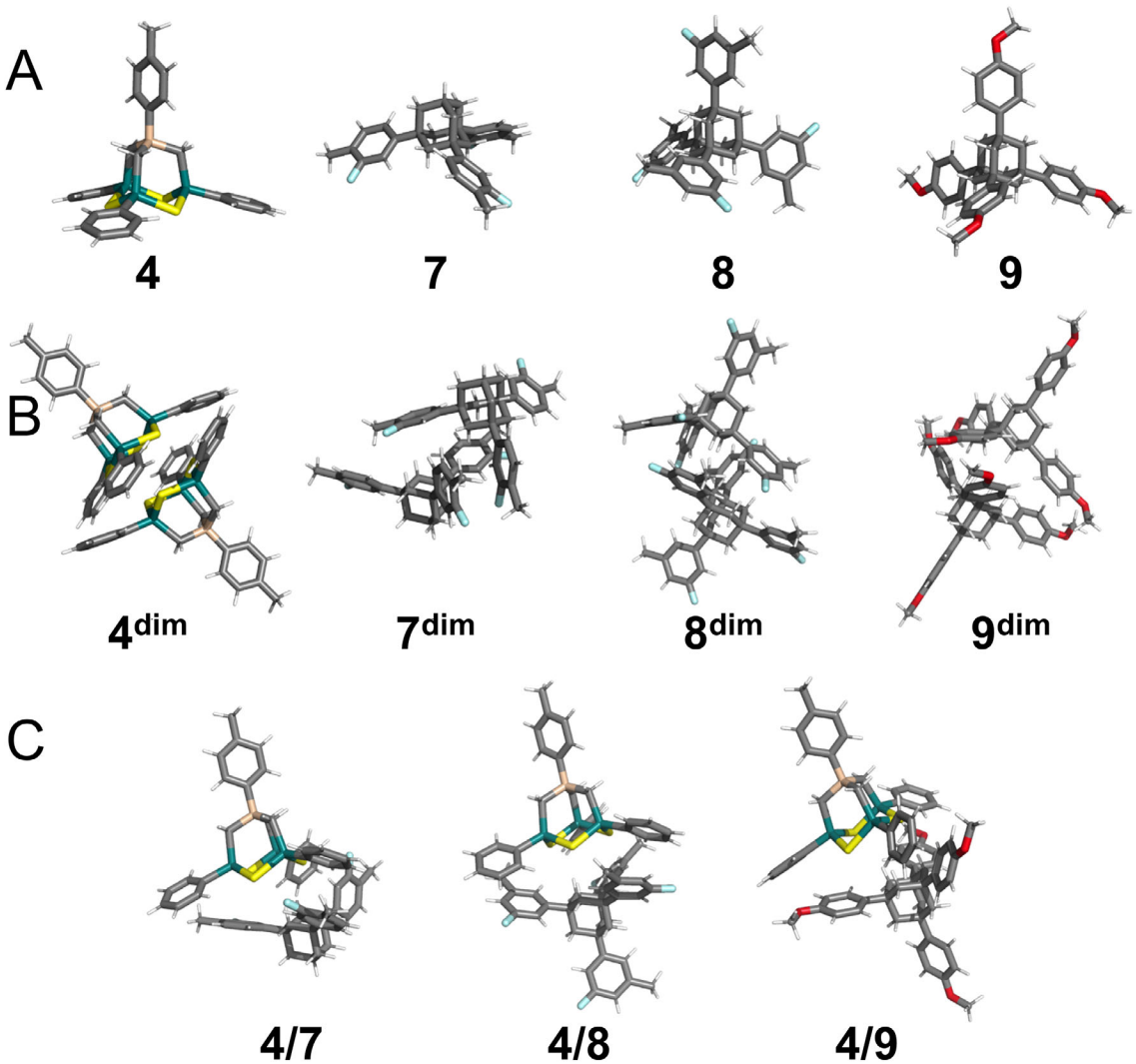


FIGURE 6 | Molecular structures of clusters and cluster pairs optimized at the B3LYP-D4/cc-pVDZ(-PP) level of theory A: Minimum-energy structures of monomers of **4**, **7**, **8**, and **9**. B: Minimum-energy structures of the "homogeneous pairs," denoted as $\mathbf{4}^{pair}$, $\mathbf{7}^{pair}$, $\mathbf{8}^{pair}$, and $\mathbf{9}^{pair}$. C: Minimum-energy structures of 'mixed pairs' of cluster **4** with **7**, **8**, and **9**, respectively. Gray: carbon, green: tin, yellow: sulfur, brown: silicon, light blue: fluoride, red: oxygen.

observation to the inhomogeneity of the film thickness that also hinders quantitative analysis of the nonlinear response and the quantum yield. As shown in previous works [2], the efficiency of this type of molecular amorphous materials is around 10–12%, but it has not been possible to explore the quantum yields. This can be explained by the fact that the nonlinear effect is not related to emitting centers, but it is a response of the material as a whole entity. In comparison to up-conversion by materials doped with rare-earth elements, the nonlinear WLG is therefore much more depending on the interaction length of the driving laser with the material. This interaction length is mainly determined by the thickness of the sample. For the case of powdery samples, the actual grain size of the powder has an additional influence on the efficiency, and scattering additionally hampers quantitative studies.

3 | Conclusion

Besides the synthesis and characterization of novel compounds [(p-$MeC_6H_4Si(CH_2SnPhE)_3$] (**4**, E = S; **5**, E = Se, **6**, E = Te), we have shown in this work that organic and inorganic adamantane-type compounds with strongly nonlinear optical properties can be combined in a physical blend. The different species retain their chemical identity during this process, but together form eutectic mixtures with lowered melting

16136829, 0, Downloaded from https://onlinelibrary.wiley.com/doi/10.1002/smll.75964 by Karlsruher Institut Fur Technologie, Wiley Online Library on [03/11/2026]. See the Terms and Conditions (https://onlinelibrary.wiley.com/terms-and-conditions) on Wiley Online Library for rules of use; OA articles are governed by the applicable Creative Commons License

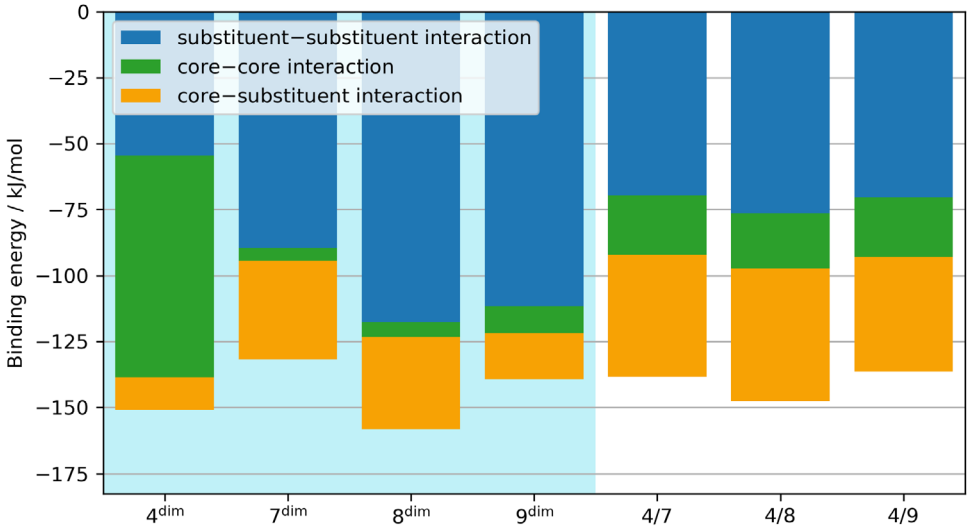


FIGURE 7 | Decomposition study of the binding energy contributions of the global minimum-energy cluster pairs into substituent–substituent (blue), core–core (green), and substituent-core (orange) interactions. Results for "homogeneous pairs" are drawn on light blue background, results for the "mixed pairs" are shown on white background.

TABLE 2 | Binding energies of "mixed pairs" **4/7**, **4/8**, and **4/9** (ΔE_{bind}), average binding energies of the mixed pairs as compared to "homogeneous pairs" of monomer clusters **4** and X = **7**, **8**, or **9** ($\Delta E^{av.}_{bind}$), and the corresponding energy differences ($\Delta\Delta E_{bind}$). All values are given in kJ mol^{-1}.

Mixed pair	ΔE_{bind}	$\Delta E^{av.}_{bind}$ [a]	$\Delta\Delta E_{bind}$ [b]
4/7	−138	−141	3
4/8	−148	−155	7
4/9	−136	−145	9

[a] $\Delta E^{av.}_{bind}\ (4/X) = \frac{1}{2} * [\Delta E_{bind}(4^{pair}) + \Delta E_{bind}(X^{pair})]$;
[b] $\Delta\Delta E_{bind}\ (4/X) = \Delta E_{bind}\ (4/X) - \Delta E^{av.}_{bind}(4/X)$.

temperatures as compared to those of the two parent compounds. For this study the sulfide cluster **4** was used for the formation of the eutectic mixtures with (3-F-4-Me-C_6H_3)$_3$Ad (**7**), (3-F-4-Me-Ph)$_4$Ad (**8**), and (4-MeO-C_6H_4)$_4$Ad (**9**). The composites **4/7** and **4/9** demonstrate great compatibility between inorganic and organic adamantane-type materials, thus generating very homogeneous mixtures with notably decreased melting temperatures. They form glassy phases upon melting and subsequent quick cooling. The materials retain the strongly non-linear optical properties upon mixing, which was also confirmed by quantum chemical investigations. The findings give rise to great potential for future applications of such materials at low cost.

4 | Experimental Section

4.1 | Reagents and Solvents

All solvents were dried by standard methods. Trichloro(phenyl)silane, *p*-tolylchlorosilane, bromochloromethane, triphenyltin chloride, hydrogen chloride, *n*-butyllithium and sodium were purchased from commercial sources.

4.2 | Instrumental Methods

Elemental analyses of H, C, and S were carried out on a CHN(S)-Analyzer vario MICRO CUBE using samples dried under reduced pressure (1×10^{-3} mbar) for 5 h. Melting temperatures were determined in a glass tube on a Krüss KSP1N melting-point apparatus. The infrared spectra were recorded on a Bruker Tensor 37 spectrometer with ATR unit. The 1D (^{1}H, ^{13}C, ^{29}Si, ^{119}Sn) and 2D (COSY, HSQC, HMBC) NMR studies were recorded at room temperature on Bruker DRX 300 and DRX 500 spectrometers. Standard internal and external references were used: tetramethylsilane (δ ^{1}H = 0, δ ^{13}C = 0 and δ ^{29}Si = 0) and tetramethyltin (δ ^{119}Sn = 0). HR-ESI mass spectra were recorded on an LTQ-FT Ultra mass spectrometer (Thermo Fischer Scientific) with $CHCl_3$/MeCN as the mobile phase. Energy-dispersive X-ray (EDX) spectroscopy was performed using the EDX detector XFlash 5010 of Bruker Nano GmbH coupled with the scanning electron microscope Jeol JIB-4610F. For scanning electron microscopy (SEM), a Jeol JIB-4601F microscope was employed. Power X-ray diffraction (PXRD) studies were carried out on a Stoe STADI MP X-ray powder diffractometer. The data for the X-ray structural analyses were collected at 100(2) K with Mo-Kα radiation (λ = 0.7107 Å) on an imaging plate detector system Stoe IPDS II using X-AREA v1.88. The structures were solved by ShelXT15 [72]. The refinement was done by full-matrix-least-squares methods against F^2 with the program ShelXL using Olex2 v1.3.0 software [72]. Structure solution and refinement data are summarized in Table S1, selected structural parameters are listed in Table S1. The TGA/DSC measurements were performed simultaneously on a METTLER TOLEDO with a heating rate of 10 K min^{-1} in N_2 atmosphere in an Al_2O_3 crucible. The compounds decompose slowly above 593–673 K in an exothermic process. The decomposition is also observable optically by the generation of a black powder. The mass loss is presumably dominated by organic fragments. Visual inspection of products in capillaries was done with a stereo light microscope SteREO Discovery.V8 by Carl Zeiss. The microscope was equipped with a high-intensive cold-light source CL 1500 ECO, an Achromat S 0.63x objective

16136829, 0, Downloaded from https://onlinelibrary.wiley.com/doi/10.1002/smll.75964 by Karlsruher Institut Fur Technologie, Wiley Online Library on [03/11/2026]. See the Terms and Conditions (https://onlinelibrary.wiley.com/terms-and-conditions) on Wiley Online Library for rules of use; OA articles are governed by the applicable Creative Commons License

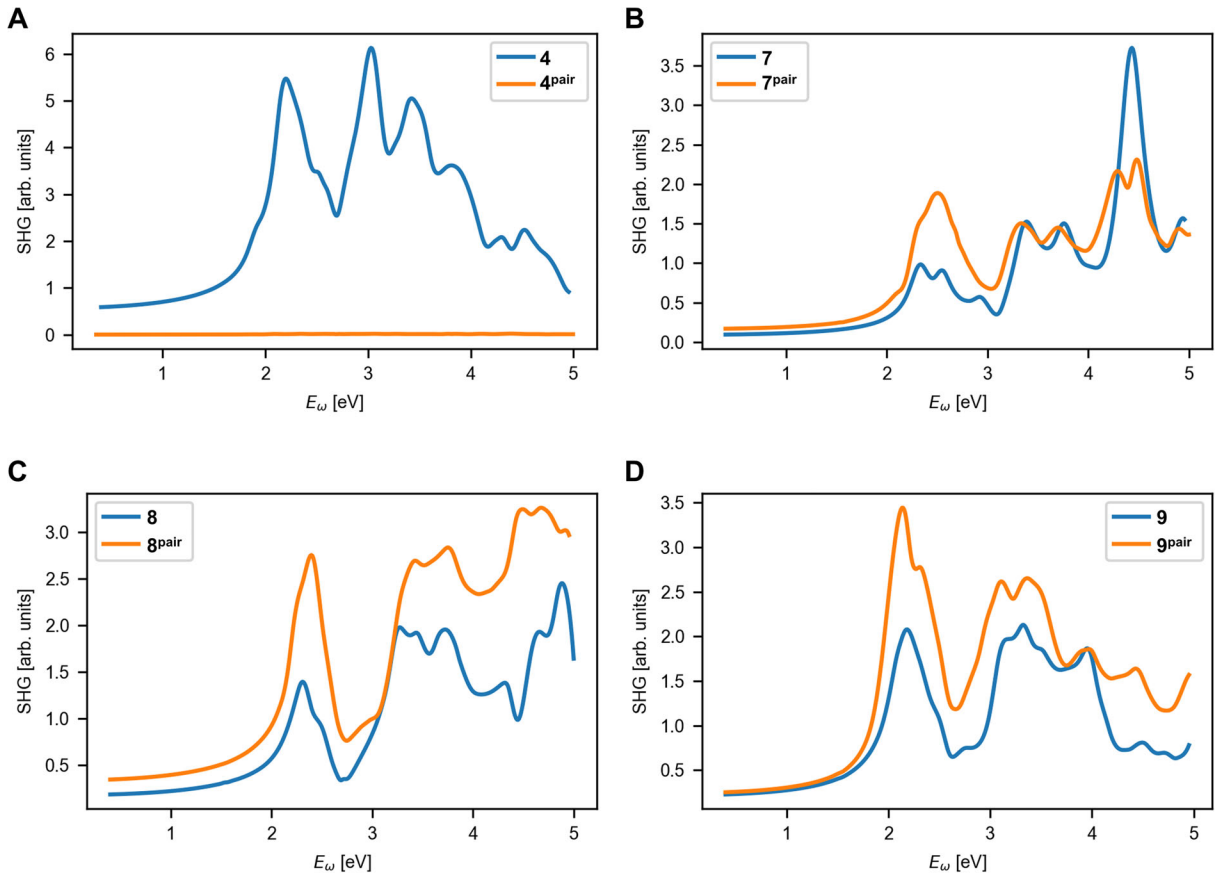


FIGURE 8 | Comparison of the calculated SHG spectra of the monomer structures **4** (A), **7** (B), **8** (C), and **9** (D) and their respective homogeneous pairs. The average of the absolute value of the $\chi^{(2)}$ SHG tensor is shown. For compound **4**, the pair formation leads to a centrosymmetric configuration with vanishing SHG, while for compounds **7**, **8**, and **9** the pair formation retains the non-centrosymmetric configuration and the optical nonlinearity.

(FWD 107 mm), a PL 10x/21 Br ocular, and an AxioCam MRc 5 camera with a 60N-C 2/3" 0,63x adapter. The raw photo material was examined by the AxioVision40 × 64 4.9.1 SP1 software. Transmission electron microscopy (TEM) was performed on a JEOL JEM-3010 microscope operated at an accelerating voltage of 300 kV and equipped with a TVIPS X416F-ES 4K camera. Powder samples were directly deposited onto 400-mesh copper grids coated with a lacey carbon film and supported by a 3 nm amorphous carbon layer.

4.3 | Synthesis and Characterization of Trichloro(*p*-tolyl)silane *p*-MePhSi(CH_2Cl)$_3$ (1)

A solution of *p*-MePhSiCl_3 (5.0 g, 22.2 mmol) in dry THF (400 mL) and BrCH_2Cl (8.6 g, 66.2 mmol) under argon atmosphere was cooled to -78°C, whereupon 26.6 mL (66.2 mmol) of a 2.5 M solution of *n*-butyllithium in hexane/THF (200 mL) were added during 1 h (the *n*-butyllithium solution was added via a special horizontally elongated side neck of the three-necked flask, which itself was immersed in the cooling bath to ensure pre-cooling of the *n*-butyllithium solution before making contact with the reaction mixture). The solution was warmed to room temperature and stirred for 12 h, then hydrolyzed and the product extracted with dichloromethane. After removal of the solvent, the residue was re-dissolved in hexane and purified by column chromatography using hexane as eluent. Subsequent elimination of the solvent under reduced pressure (1×10^{-3} mbar) yielded 2.67 g (45%). ^{29}Si{^{1}H} NMR ($CDCl_3$, 79.5 MHz, 298 K) δ: -8.62 ppm. ^{1}H NMR ($CDCl_3$, 400.2 MHz, 298 K) δ: 3.32 (s, 6H, $SiCH_2$), 2.43 (s, 3H, CH_3) 7.29–7.62 (dd, 4H, $C_{12}H_8$) ppm. ^{13}C{^{1}H} NMR ($CDCl_3$, 100.6 MHz, 298 K) δ: 24.7 ($SiCH_2$), 21.8 (CH_3), 134.8 (C1), 134.7 (C2), 129.4 (C3), 141.7 (C4) ppm.

4.4 | Synthesis and Characterization of *p*-Tolyltris((triphenylstannyl)methyl)silane *p*-MePhSi(CH_2SnPh_3)$_3$ (2)

A solution of Ph_3SnCl (10.8 g, 27.9 mmol) in dry THF (400 mL), sodium (0.64 g, 27.9 mmol) and catalytic amounts of naphthalene were placed under argon atmosphere into a 500 mL three-necked flask equipped with a magnetic stirring bar. The reaction mixture was stirred for 3 d, after that the reaction mixture was filtered whereupon the solution was cooled to 78°C followed by dropwise addition of a solution of *p*-Me*PhSi*(CH_2Cl)$_3$ (2.5 g, 9.3 mmol) in 50 mL of THF. After stirring for 12 h, the solvent was distilled off and the residue re-dissolved in 200 mL of CH_2Cl_2. Then, the reaction mixture was hydrolyzed and the organic layer extracted with CH_2Cl_2, dried over $MgSO_4$, and filtered. After removal of the solvent, the residue was washed with hexane (3×25 mL) and dried under reduced pressure (1×10^{-3} mbar) to yield 2.0 g (5.0 mmol, 90%). IR ν_{max}: 445 (s), 549 (w), 630 (m), 631 (m), 697 (s), 726 (s), 747 (s), 802 (w), 854 (w), 910 (w), 952 (w), 996 (m), 1006

16136829, 0, Downloaded from https://onlinelibrary.wiley.com/doi/10.1002/smll.75964 by Karlsruher Institut Fur Technologie, Wiley Online Library on [03/11/2026]. See the Terms and Conditions (https://onlinelibrary.wiley.com/terms-and-conditions) on Wiley Online Library for rules of use; OA articles are governed by the applicable Creative Commons License

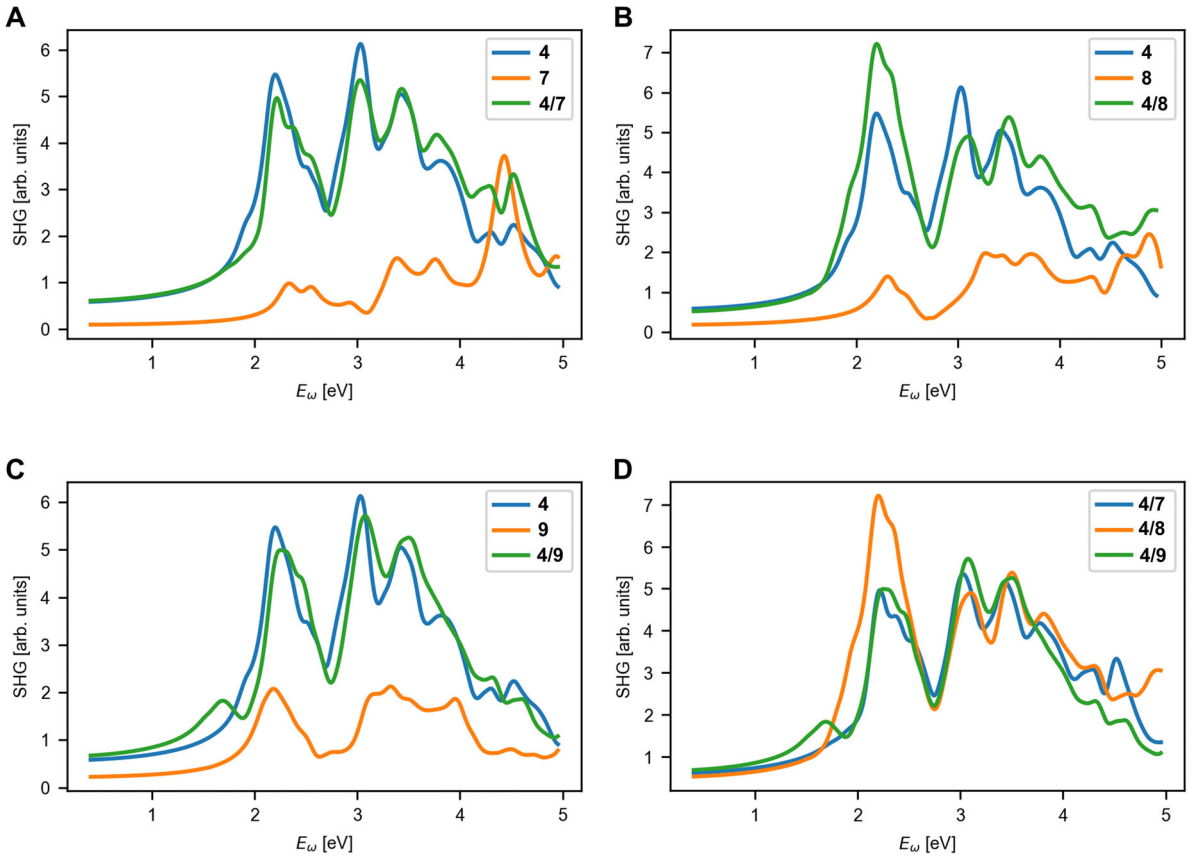


FIGURE 9 | Comparison of the calculated SHG spectra of the mixed structures and their respective monomers. The average of the absolute value of the $\chi^{(2)}$ SHG tensor is shown. The SHG response of the mixed structures closely matches in each case that of a dominant cluster.

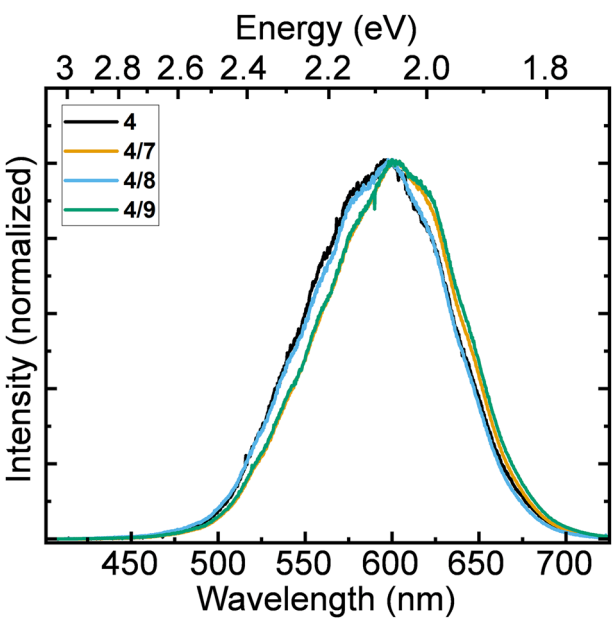


FIGURE 10 | Emission spectrum of **4** (black line) and mixtures of **4/7** (orange line), **4/8** (blue line), **4/9** (green line) following 980 nm excitation for comparison the spectra are normalized to the same intensity at 750 nm. To convey the color impression, the emission is plotted as photometric spectrum, i.e., as perceived under photopic vision (see main text for details).

(m), 1021 (m), 1074 (m), 1102 (m), 1156 (w), 1190 (w), 1258 (w), 1299 (w), 1332 (w), 1427 (s), 1480 (m), 1596 (w), 1642 (w), 1771 (w), 1816 (w), 1876 (w), 1951 (w), 2864 (w), 2987 (w), 3009 (w), 3041 (w), 3061 (w) cm^{-1}.$^{119}Sn\{^1H\}$ NMR ($CDCl_3$, 111.9 MHz, 300 K) δ: -92.5 ppm. $^{29}Si\{^1H\}$ NMR ($CDCl_3$, 59.6 MHz, 300 K) δ: 3.11 ppm. ^1H NMR ($CDCl_3$, 300.1 MHz, 300 K) δ: 0.54 (s, 6H, $SiCH_2$), 2.27 (s, 3H, CH_3), 6.69–6.72 (dd, 4H, $H_{aromatic}$), 7.01-7.29 (m, 45H, $H_{aromatic}$) ppm. $^{13}C\{^1H\}$ NMR ($CDCl_3$, 75.5 MHz, 300 K) δ: –2.4 ($SiCH_2$), 21.5 (CH_3), 139.7 (C1'), 134.2 (C2'), 128.4 (C3'), 137.1 (C4'), 128.8 (C_p), 128.7 (C_m), 137.4 (C_o), 139.7 (C_i) ppm. CHNS anal. calcd. for $C_{64}H_{58}SiSn_3$ (1211.4 g mol^{-1}): C, 63.5; H, 4.8. Found: C, 63.5; H, 4.8.

4.5 | Synthesis and Characterization of Tris((dichloro(phenyl)stannyl)methyl)(*p*-tolyl)silane *p*-$MePhSi(CH_2SnPhCl_2)_3$ (3)

2.0 g of precursor *p*-$MePhSi(CH_2SnPh_3)_3$ (1.65 mmol) and 50 mL of dichloromethane were placed into a 100 mL ball flask equipped with a magnetic stirring bar. The solution was cooled to 0°C, whereupon 2 M of HCl in ether (4.9 mL, 9.9 mmol) was added drop by drop during 60 min. The reaction mixture was allowed to stir for 12 h. Subsequently, the solvent was evaporated and the byproduct (benzene) removed under reduced pressure (1×10^{-3} mbar) to give precursor **3** as a viscous brown compound in 50% yield (0.79 g, mmol). IR ν_{max}: 443 (s), 490 (w), 558 (m), 631 (s),

16136829, 0, Downloaded from https://onlinelibrary.wiley.com/doi/10.1002/smll.75964 by Karlsruher Institut Fur Technologie, Wiley Online Library on [03/11/2026]. See the Terms and Conditions (https://onlinelibrary.wiley.com/terms-and-conditions) on Wiley Online Library for rules of use; OA articles are governed by the applicable Creative Commons License

664 (s), 691 (s), 706 (s), 727 (s), 802 (w), 848 (w), 915 (w), 997 (m), 1028 (m), 1071 (m), 1104 (m), 1192 (w), 1262 (w), 1333 (w), 1357 (w), 1432 (s), 1480 (w), 1578 (w), 1598 (w), 1648 (w), 1815 (w), 2947 (w), 3023 (w), 3049 (w), 3069 (w) cm^{-1}. ^{1}H NMR ($CDCl_3$, 300.1 MHz, 300 K) δ: 1.66 (s, 6H, $SiCH_2$), 2.33 (s, 3H, CH_3), 7.20–7.58 (m, 19H, $H_{aromatic}$) ppm. CHNS anal. calcd. for $C_{28}H_{28}Cl_6SiSn_3$ (961.5 g mol^{-1}): C, 34.9; H, 2.9. Found: C, 34.9; H, 3.2.

4.6 | Synthesis and Characterization of (1s,3s,5s)-1,3,5-Triphenyl-7-(*p*-tolyl)-2,4,9-trithia-7-sila-1,3,5-tristannaadamantane *p*-MePhSi(CH_2PhS)$_3$ (4)

To a solution of *p*-MePhSi(CH_2PhCl_2)$_3$ (0.5 g, 0.52 mmol) in 20 mL of dry toluene were added 0.28 g (1.56 mmol) of TMS_2S, and the reaction mixture was stirred at room temperature for 24 h. After the solvent was removed under reduced pressure (1×10^{-3} mbar), the solid was washed three times with dry hexane and filtered to give the product in 55% yield (0.24 g, 0.29 mmol). m. p.: 192–202 °C. IR ν_{max}: 444 (s), 483 (m), 538 (s), 619 (w), 659 (s), 687 (s), 724 (s), 753 (s), 799 (w), 844 (w), 910 (w), 976 (m), 1005 (m), 1072 (m), 1102 (m), 1189 (w), 1253 (w), 1299 (w), 1313 (w), 1330 (w), 1344 (w), 1390 (w), 1430 (m), 1479 (w), 1577 (w), 1599 (w), 1638 (w), 1814 (w), 2883 (w), 2938 (w), 3010 (w), 3040 (w), 3063 (w) cm^{-1}. $^{119}Sn\{^{1}H\}$ NMR ($CDCl_3$, 186.5 MHz, 300 K) δ: 100.7 ppm. $^{29}Si\{^{1}H\}$ NMR ($CDCl_3$, 99.4 MHz, 300 K) δ: 4.69 ppm. ^{1}H NMR ($CDCl_3$, 500.2 MHz, 300 K) δ: 1.01 (s, 6H, $SiCH_2$), 2.37 (s, 3H, *p*-MePhSi), 7.49-7.74 (m, 19H, $H_{aromatic}$) ppm. $^{13}C\{^{1}H\}$ NMR ($CDCl_3$, 125.8 MHz, 300 K) δ: 4.2 ($SiCH_2$), 21.5 (*p*-MePhSi), 139.6 (C1'), 132.3 (C2'), 129.0 (C3'), 138.4 (C4'), 130.3 (C_p), 129.1 (C_m), 134.5 (C_o), 141.4 (C_i) ppm. CHNS anal. calcd. for $C_{27}H_{26}S_3SiSn_3$ (830.9 g mol^{-1}): C, 39.0; H, 3.2; S, 11.5. Found: C, 37.8; H, 3.4; S, 11.1. MS (ESI^-) for $[C_{27}H_{26}ClS_3SiSn_3]^-$ $[M+Cl]^-$: *m/z* (exp.) = 864.7743, *m/z* (calcd.) = 864.7709.

4.7 | Synthesis and Characterization of (1s,3s,5s)-1,3,5-Triphenyl-7-(*p*-tolyl)-2,4,9-triselena-7-sila-1,3,5-tristannaadamantane *p*-MePhSi(CH_2PhSe)$_3$ (5)

To a solution of *p*-MePhSi(CH_2PhCl_2)$_3$ (0.5 g, 0.52 mmol) in 20 mL of dry toluene were added 0.35 g (1.56 mmol) of TMS_2Se, and the reaction mixture was stirred at room temperature 24 h. After the solvent was removed under reduced pressure (1×10^{-3} mbar), the solid was washed three times with dry hexane and filtered to give the product in 65% yield (0.33 g, 0.34 mmol). m. p.: 201–206 °C. IR ν_{max}: 441 (s), 481 (w), 532 (s), 656 (s), 688 (s), 724 (s), 755 (s), 797 (w), 843 (w), 908 (w), 975 (m), 1004 (m), 1070 (m), 1101 (m), 1253 (w), 1297 (w), 1312 (w), 1329 (w), 1341 (w), 1390 (w), 1429 (w), 1499 (w), 1575 (w), 1599 (w), 1808 (w), 2877 (w), 2929 (w), 3008 (w), 3037 (w), 3059 (w) cm^{-1}. $^{119}Sn\{^{1}H\}$ NMR ($CDCl_3$, 186.5 MHz, 300 K) δ: 5.0 ppm. $^{29}Si\{^{1}H\}$ NMR ($CDCl_3$, 99.4 MHz, 300 K) δ: 5.0 ppm. $^{77}Se\{^{1}H\}$ NMR ($CDCl_3$, 95.4 MHz, 300 K) δ: -349 ppm. ^{1}H NMR ($CDCl_3$, 500.2 MHz, 300 K) δ: 1.15 (s, 6H, $SiCH_2$), 2.40 (s, 3H, *p*-MePhSi), 7.40–7.67 (m, 19H, $H_{aromatic}$) ppm. $^{13}C\{^{1}H\}$ NMR ($CDCl_3$, 75.5 MHz, 300 K) δ: 4.0 ($SiCH_2$), 21.5 (*p*-MePhSi), 139.5 (C1'), 132.3 (C2'), 129.0 (C3'), 139.3 (C4'), 130.2 (C_p), 129.0 (C_m), 134.5 (C_o), 140.6 (C_i) ppm. CHNS anal. calcd. for $C_{27}H_{26}Na_3SiSn_3$ (985.6 g mol^{-1}): C, 34.1; H, 2.8. Found: C, 32.5; H, 3.0. MS (ESI^-) for $[C_{27}H_{26}ClS_3SiSn_3]^-$ $[M+Na]^+$: *m/z* (exp.) = 1008.6434, *m/z* (calcd.) = 1008.6443.

4.8 | Synthesis and Characterization of (1s,3s,5s)-1,3,5-Triphenyl-7-(p-tolyl)-2,4,9-tritellura-7-sila-1,3,5-tristannaadamantane p-MePhSi(CH_2PhTe)$_3$ (6)

To a solution of *p*-MePhSi(CH_2PhCl_2)$_3$ (0.5 g, 0.52 mmol) in 20 mL of dry toluene were added 0.42 g (1.56 mmol) of TMS_2Te, and the reaction mixture was stirred at room temperature 24 h. After the solvent was removed under reduced pressure (1×10^{-3} mbar), the solid was washed three times with dry hexane and filtered to give the product in 80% yield (4.1 g, 4.5 mmol). IR ν_{max}: 414 (w), 441 (s), 478 (w), 521 (s), 615 (m), 649 (s), 688 (s), 723 (s), 753 (s), 796 (w), 841 (w), 906 (w), 974 (m), 995 (m), 1068 (m), 1098 (m), 1156 (w), 1187 (w), 1248 (w), 1294 (w), 1328 (w), 1338 (w), 1388 (w), 1427 (m), 1476 (w), 1499 (w), 1573 (w), 1598 (w), 1804 (w), 1867 (w), 1887 (w), 1944 (w), 1963 (w), 2869 (w), 2917 (w), 3005 (w), 3032 (w), 3058 (w) cm^{-1}. $^{119}Sn\{^{1}H\}$ NMR ($CDCl_3$, 112 MHz, 300 K) δ: –246 ppm [$^{1}J(^{125}Te–^{117/119}Sn)$ = 3066 Hz]. $^{29}Si\{^{1}H\}$ NMR ($CDCl_3$, 59.6 MHz, 300 K) δ: 5.5 ppm. $^{125}Te\{^{1}H\}$ NMR ($CDCl_3$, 157.8 MHz, 300 K) δ: –864 ppm [$^{1}J(^{117/119}Sn–^{125}Te)$ = 3069/2929 Hz]. ^{1}H NMR ($CDCl_3$, 500.1 MHz, 300 K) δ: 1.35 (s, 6H, $SiCH_2$), 2.34 (s, 3H, *p*-MePhSi), 7.19–7.64 (m, 19H, $H_{aromatic}$) ppm. $^{13}C\{^{1}H\}$ NMR ($CDCl_3$, 75.5 MHz, 300 K) δ: 2.9 ($SiCH_2$), 21.6 (*p*-MePhSi) 141.0 (C1'), 130.1 (C2'), 129.0 (C3'), 130.1 (C4'), 130.1 (C_p), 128.9 [$^{3}J(^{13}C–^{117/119}Sn)$ = 51.4 Hz, C_m], 134.9 [$^{2}J(^{13}C–^{117/119}Sn)$ = 52.9 Hz, C_o], 137.5 (C_i) ppm. μ-XFS: Si/Sn/Te ratio for $C_{28}H_{28}Si_1Sn_4Te_3$: 14.2, 42.9, 42.9 at-%. Si/Sn/Te ratio found: 10.6, 43.4, 46.0 at-%. MS (ESI^-) for $[C_{27}H_{26}ClS_3SiSn_3]^-$ ($[M+Cl]^-$): *m/z* (exp.) = 1166.5863, *m/z* (calcd.) = 1166.5862.

4.9 | Synthetic Procedures for Adamantane Derivatives

The syntheses of (3-F-4-Me-C_6H_3)$_3$Ad (**7**), (3-F-4-Me-Ph)$_4$Ad (**8**), and (4-MeO-C_6H_4)$_4$Ad (**9**) were carried out using published methods [53, 54].

4.10 | Computational Details

4.10.1 | Structural and Energy Decomposition Analyses

The structures of the chemical systems under investigation were generated using our in-house developed Python module ClusterMaster. Based on the optimized monomers (compounds **4**–**9**), the pair structures were created by placing two monomers near each other resulting in four pair of the same compound (homogeneous pairs $\mathbf{4}^{pair}$, $\mathbf{7}^{pair}$, $\mathbf{8}^{pair}$, and $\mathbf{9}^{pair}$) and three mixed pairs (heterogeneous pairs **4/7**, **4/8**, and **4/9**). A search for the most energetically stable conformers of four monomer and seven dimer structures was performed at the GFN2-xTB level of theory [73–75] with the use of the iterative meta-dynamics with genetic structure crossing (iMTG-GC) algorithm [76], as implemented in CREST [77] and an energy window of 21.1 kJ mol^{-1}. The

16136829, 0, Downloaded from https://onlinelibrary.wiley.com/doi/10.1002/smll.75964 by Karlsruher Institut Fur Technologie, Wiley Online Library on [03/11/2026]. See the Terms and Conditions (https://onlinelibrary.wiley.com/terms-and-conditions) on Wiley Online Library for rules of use; OA articles are governed by the applicable Creative Commons License

resulting minimum-energy structures were then optimized at the B3LYP-D4/cc-pVDZ(-PP) [78–87] level of theory including the ECP28MDF pseudopotential for Sn [88, 89] using the program system Turbomole 7.5 [90]. A vibrational frequency analysis performed using NumForce module confirmed all structures to be minima according to the absence of any imaginary frequencies for the optimized structures. After structure optimization and frequency analysis, the binding energies of the systems were decomposed into different contributions employing B3LYP-D4/cc-pVDZ(-PP) computational approach [25, 26, 37].

4.10.2 | Calculation of Nonlinear Optical Response

Nonlinear optics calculations were performed in the real time approach within the independent particle approximation as implemented in the YAMBO code [70, 91] using the equilibrium structures of monomers and dimers reoptimized by PAW PBE-D3(BJ) method [66–69, 92] in combination with the optimized norm-conserving Vanderbilt pseudopotentials [93, 94]. Numerical parameters, such as time-step, total propagation time, or spectral broadening, are chosen to ensure convergence of the nonlinear optical spectra and can be found elsewhere. The ground-state electronic structure, upon which the calculation of the nonlinear optical response is based, is calculated with DFT with the plane-wave code QuantumEspresso [95].

Author Contributions

Irán Rojas-león: investigation, methodology, validation, visualization, writing – original draft, conceptualization. **Jan Christmann**: investigation, validation, writing – original draft. **Saravanan Gowrisankar**: investigation, writing – original draft, validation, visualization. **Sebastian Schwan**: investigation, validation, visualization, writing – original draft. **Anton S. Nizovtsev**: investigation, writing – original draft, validation. **Ferdinand Ziese**: investigation, writing – original draft, validation, visualization. **Jürgen Belz**: investigation, validation, writing – original draft. **Johannes Haust**: investigation, writing – original draft, validation. **Jihed Ayari**: investigation, validation, writing – original draft. **Kerstin Volz**: writing – original draft, supervision, funding acquisition. **Nils W. Rosemann**: investigation, writing – original draft, validation, visualization, funding acquisition. **Simone Sanna**: writing – original draft, writing – review and editing, supervision, funding acquisition. **Doreen Mollenhauer**: writing – original draft, writing – review and editing, supervision, funding acquisition. **Klaus Jurkschat**: writing – original draft, writing – review and editing, supervision. **Peter R. Schreiner**: writing – original draft, writing – review and editing, supervision, funding acquisition. **Stefanie Dehnen**: conceptualization, funding acquisition, writing – original draft, writing – review and editing, visualization, supervision, project administration.

Acknowledgements

Open access funding enabled and organized by Projekt DEAL.

Conflicts of Interest

The authors declare no conflicts of interest.

Data Availability Statement

The data that support the findings of this study are available from the corresponding author upon reasonable request.

References

1. J. Wu, G. Zheng, X. Liu, and J. Qiu, "Near-infrared Laser Driven White Light Continuum Generation: Materials, Photophysical Behaviours and Applications," *Chemical Society Reviews* 49 (2020): 3461–3483, https://doi.org/10.1039/c9cs00646j.

2. N. W. Rosemann, J. P. Eußner, A. Beyer, et al., "A Highly Efficient Directional Molecular White-Light Emitter Driven by a Continuous-Wave Laser Diode," *Science* 352 (2016): 1301–1304, https://doi.org/10.1126/science.aaf6138.

3. P. Osewski, A. Belardini, E. Petronijevic, et al., "Self-Phase-Matched Second-Harmonic and White-Light Generation in a Biaxial Zinc Tungstate Single Crystal," *Scientific Reports* 7 (2017): 45247, https://doi.org/10.1038/srep45247.

4. J. Gotta, T. B. Shalom, S. Aslanoglou, et al., "Stable White Light-Emitting Biocomposite Films," *Advanced Functional Materials* 28 (2018): 1706967, https://doi.org/10.1002/adfm.201706967.

5. H. Su, Y. Chen, and K. Wong, "Recent Progress in White Light-Emitting Electrochemical Cells," *Advanced Functional Materials* 30 (2020): 1906898, https://doi.org/10.1002/adfm.201906898.

6. X. Lu, G. Moille, A. Rao, and D. A. Westly, "Efficient Photoinduced Second-harmonic Generation in Silicon Nitride Photonics," *Nature Photonics* 15 (2021): 131–136, https://doi.org/10.1038/s41566-020-00708-4.

7. J. Zhao, A. Fieramosca, R. Bao, et al., "Nonlinear Polariton Parametric Emission in an Atomically Thin Semiconductor Based Microcavity," *Nature Nanotechnology* 17 (2022): 396–402, https://doi.org/10.1038/s41565-022-01073-9.

8. D. A. Akimov, M. Schmitt, R. Maksimenka, et al., "Supercontinuum Generation in a Multiple-submicron-core Microstructure fiber: Toward Limiting Waveguide Enhancement of Nonlinear-Optical Processes," *Applied Physics B* 77 (2003): 299–305, https://doi.org/10.1007/s00340-003-1200-0.

9. M. Guignard, V. Nazabal, J. Troles, et al., "Second-Harmonic Generation of Thermally Poled Chalcogenide Glass," *Optics Express* 13 (2005): 789–795, https://doi.org/10.1364/OPEX.13.000789.

10. J. He, M. Zeller, A. D. Hunter, and Z. Xu, "White Light Emission and Second Harmonic Generation from Secondary Group Participation (SGP) in a Coordination Network," *Journal of the American Chemical Society* 134 (2012): 1553–1559, https://doi.org/10.1021/ja2073559.

11. W.-H. Lai, A. S. Haynes, L. Frazer, et al., "Situ Probing of the Mechanisms of Coking Resistance on Catalyst-Modified Anodes for Solid Oxide Fuel Cells," *Chemistry of Materials* 27 (2015): 822–828, https://doi.org/10.1021/cm503852v.

12. G. Li, Q. Liu, K. Wu, Z. Yang, and S. Pan, "$Na_2CdGe_2Q_6$ (Q = S, Se): Two Metal-Mixed Chalcogenides with Phase-Matching Abilities and Large Second-Harmonic Generation Responses," *Dalton Transactions* 46 (2017): 2778–2784, https://doi.org/10.1039/c7dt00087a.

13. R. R. Alfano, *The Supercontinuum Laser Source* (Springer, 2006).

14. S. Parola, B. Julián-López, L. D. Carlos, and C. Sanchez, "Optical Properties of Hybrid Organic-Inorganic Materials and their Applications," *Advanced Functional Materials* 26 (2016): 6506–6544, https://doi.org/10.1002/adfm.201602730.

15. Y. Kang and Q. Wu, "A Review of the Relationship between the Structure and Nonlinear Optical Properties of Organic-Inorganic Hybrid Materials," *Coordination Chemistry Reviews* 498 (2024): 215458, https://doi.org/10.1016/j.ccr.2023.215458.

16. E. Cariati, R. Macchi, D. Roberto, et al., "Polyfunctional Inorganic–Organic Hybrid Materials: An Unusual Kind of NLO Active Layered Mixed Metal Oxalates with Tunable Magnetic Properties and Very Large Second Harmonic Generation," *Journal of the American Chemical Society* 129 (2007): 9410–9420, https://doi.org/10.1021/ja0710712.

17. S.-P. Zhao and X.-M. Ren, "Toward Design of Multiple-Property Inorganic–Organic Hybrid Compounds Based on Face-Sharing Octahe-

16136829, 0, Downloaded from https://onlinelibrary.wiley.com/doi/10.1002/smll.75964 by Karlsruher Institut Fur Technologie, Wiley Online Library on [03/11/2026]. See the Terms and Conditions (https://onlinelibrary.wiley.com/terms-and-conditions) on Wiley Online Library for rules of use; OA articles are governed by the applicable Creative Commons License

dral Iodoplumbate Chains," *Dalton Transactions* 40 (2011): 8261–8272, https://doi.org/10.1039/c0dt01806f.

18. E. Ferreira, G. Ramos-Ortiz, A. Vazquez, and M. Trejo-Durán, "Third-order Nonlinear Optical Properties of Choline Chloride Based Deep Eutectic Solvents: Theoretical and Experimental Studies," *Journal of Molecular Liquids* 384 (2023): 122253, https://doi.org/10.1016/j.molliq.2023.122253.

19. S. Wang, W. Fang, and J. Zhang, "Meltable Aluminum Molecular Rings with Fluorescence and Nonlinear Optical Properties," *Angewandte Chemie International Edition* 63 (2024): 202400161, https://doi.org/10.1002/anie.202400161.

20. E. Ferreira, J. E. Castellanos-Águila, A. Vazquez, and M. Trejo-Durán, "Theorical Calculations on Nonlinear Optical Properties of Choline Chloride-urea Deep Eutectic Solvent," Proc. SPIE Nonlinear Optics and Applications XII, 117701T (18 Apr 2021), 11770, https://doi.org/10.1117/12.2592264.

21. A. A. Fokin, M. Šekutor, and P. R. Schreiner, *The Chemistry of Diamondoids: Building Blocks for Ligands, Catalysts, Materials, and Pharmaceuticals* (Wiley-VCH, 2024), https://doi.org/10.1002/9783527812950.

22. N. W. Rosemann, J. P. Eußner, E. Dornsiepen, S. Chatterjee, and S. Dehnen, "Organotetrel Chalcogenide Clusters: Between Strong Second-Harmonic and White-Light Continuum Generation," *Journal of the American Chemical Society* 138 (2016): 16224–16227, https://doi.org/10.1021/jacs.6b10738.

23. E. Dornsiepen, F. Dobener, S. Chatterjee, and S. Dehnen, "Controlling the White-Light Generation of $[(RSn)_4E_6]$: Effects of Substituent and Chalcogenide Variation," *Angewandte Chemie International Edition* 58 (2019): 17041–17046, https://doi.org/10.1002/anie.201909981.

24. S. Dehnen, P. R. Schreiner, S. Chatterjee, et al., "Amorphous Molecular Materials for Directed Supercontinuum Generation," *ChemPhotoChem* 5 (2021): 1033–1041, https://doi.org/10.1002/cptc.202100130.

25. I. Rojas-León, J. Christmann, S. Schwan, et al., "Cluster-Glass for Low-Cost White-Light Emission," *Advanced Materials* 34 (2022): 2203351, https://doi.org/10.1002/adma.202203351.

26. S. Schwan, A. J. Achazi, F. Ziese, et al., "Insights into Molecular Cluster Materials with Adamantane-Like Core Structures by Considering Dimer Interactions," *Journal of Computational Chemistry* 44 (2023): 843–856, https://doi.org/10.1002/jcc.27047.

27. N. W. Rosemann, H. Locke, P. R. Schreiner, and S. Chatterjee, "White-Light Generation through Nonlinear Optical Response of 1,3,5,7-Tetraphenyladamantane: Amorphous versus Crystalline States," *Advanced Optical Materials* 6 (2018): 1701162, https://doi.org/10.1002/adom.201701162.

28. B. D. Klee, E. Dornsiepen, J. R. Stellhorn, et al., "Structure Determination of a New Molecular White-Light Source," *Physica Status Solidi (b)* 255 (2018): 1800083, https://doi.org/10.1002/pssb.201800083.

29. E. Dornsiepen, F. Dobener, N. Mengel, et al., "White-Light Generation Upon In-Situ Amorphization of Single Crystals of $[\{(Me_3P)_3AuSn\}(PhSn)_3S_6]$ and $[\{(Et_3P)_3AgSn\}(PhSn)_3S_6]$," *Advanced Optical Materials* 7 (2019): 1801793, https://doi.org/10.1002/adom.201801793.

30. J. E. Beetar, M. Nrisimhamurty, T.-C. Truong, et al., "Multioctave Supercontinuum Generation and Frequency Conversion Based on Rotational Nonlinearity," *Science Advances* 6 (2020): abb5375, https://doi.org/10.1126/sciadv.abb5375.

31. F. Meng, C. Lapre, C. Billet, et al., "Intracavity Incoherent Supercontinuum Dynamics and Rogue Waves in a Broadband Dissipative Soliton Laser," *Nature Communications* 12 (2021): 5567, https://doi.org/10.1038/s41467-021-25861-4.

32. R. Fan, Y.-Y. Lin, L. Chang, et al., "Higher Order Mode Supercontinuum Generation in Tantalum Pentoxide (Ta_2O_5) Channel Waveguide," *Scientific Reports* 11 (2021): 7978, https://doi.org/10.1038/s41598-021-86922-8.

33. H. Xiang, R. Wang, J. Chen, F. Li, and H. Zeng, "Research Progress of Full Electroluminescent White Light-emitting Diodes Based on a Single Emissive Layer," *Light: Science & Applications* 10 (2021): 206, https://doi.org/10.1038/s41377-021-00640-4.

34. J. Link Vasco, J. R. Stellhorn, B. D. Klee, et al., "Structure Determination in a New Type of Amorphous Molecular Solids with Different Nonlinear Optical Properties: a Comparative Structural Analysis," *Journal of Physics: Condensed Matter* 35 (2023): 384001.

35. J. Haust, J. Belz, M. Müller, et al., "White Light Generating Molecular Materials: Correlation between the Amorphous/Crystalline Structure and Nonlinear Optical Properties," *ChemPhotoChem* 6 (2022): 202200071, https://doi.org/10.1002/cptc.202200071.

36. J. Belz, J. Haust, M. J. Müller, et al., "Adamantanes as White-Light Emitters: Controlling the Arrangement and Functionality by External Coulomb Forces," *The Journal of Physical Chemistry C* 126 (2022): 9843–9854, https://doi.org/10.1021/acs.jpcc.2c02686.

37. K. Hanau, S. Schwan, M. R. Schäfer, et al., "Towards Understanding the Reactivity and Optical Properties of Organosilicon Sulfide Clusters," *Angewandte Chemie* 133 (2021): 1196–1206, https://doi.org/10.1002/ange.202011370.

38. B. Bureau, C. Boussard-Pledel, P. Lucas, X. Zhang, and J. Lucas, "Forming Glasses from Se and Te," *Molecules* 14 (2009): 4337–4350, https://doi.org/10.3390/molecules14114337.

39. M. A. Popescu, *Non-Crystalline Chalcogenides* (Springer, 2000).

40. A. K. Varshneya, *Fundamentals of Inorganic Glasses*, ed. A. K. Varshneya, (Academic Press, 1994).

41. J. Zarzycki, *Glasses and the Vitreous State* (Cambridge University Press, 1991).

42. A. Singh, M. K. Jana, and D. B. Mitzi, "Reversible Crystal–Glass Transition in a Metal Halide Perovskite," *Advanced Materials* 33 (2021): 2005868, https://doi.org/10.1002/adma.202005868.

43. M. M. Smedskjaer and S. S. Sørensen, "A Glass Act," *Nature Chemistry* 13 (2021): 723–724, https://doi.org/10.1038/s41557-021-00756-5.

44. Y. Huang, F. Chen, R. Lin, et al., "Glass Formation and Mid-infrared Optical Nonlinearities of Chalcogenide Glasses in Germanium-tin-sulfur Ternary System," *Optical Materials Express* 6 (2016): 3053–3062, https://doi.org/10.1364/OME.6.003053.

45. W. Tu, Z. Chen, Y. Gao, et al., "Glass Transition and Mixing Thermodynamics of a Binary Eutectic System," *Physical Chemistry Chemical Physics* 16 (2014): 3586–3592, https://doi.org/10.1039/c3cp52868e.

46. A. B. Adam, S. Sakrani, and Y. Wahab, "Glass-formation region of ternary Sn-Sb-Se-Based chalcogenide glasses," *Journal of Materials Science* 40 (2005): 1571–1576, https://doi.org/10.1007/s10853-005-0655-2.

47. D. Troegel, F. Möller, C. Burschka, and R. Tacke, "Synthesis and Characterization of New Trifunctional Tetraorganylsilanes of the Formula Types $MeSi(CH_2X)_3$, $MeSi(CH_2X)_2CH_2X'$, and $MeSi(CH_2X)(CH_2X')CH_2X''$," *Organometallics* 28 (2009): 5765–5770, https://doi.org/10.1021/om9005577.

48. J. Ayari, C. R. Göb, I. M. Oppel, M. Lutter, W. Hiller, and K. Jurkschat, "$MeSi(CH_2SnRO)_3$ (R = Ph, Me_3SiCH_2): Bausteine für Dreieckförmige Diorganozinnoxidmakrocyclen," *Angewandte Chemie* 132 (2020): 24102–24109, https://doi.org/10.1002/ange.202012248.

49. C. Shen, H. Yu, and Z. Wang, "Synthesis of 1,3,5,7-tetrakis(4-cyanatophenyl)Adamantane and Its Microporous Polycyanurate Network for Adsorption of Organic Vapors, Hydrogen and Carbon Dioxide," *Chemical Communications* 50 (2014): 11238–11241, https://doi.org/10.1039/c4cc05021e.

50. P.-E. Alexandre, A. Schwenger, W. Frey, and C. Richert, "High-Loading Crystals of Tetraaryladamantanes and the Uptake and Release of Aromatic Hydrocarbons from the Gas Phase," *Chemistry – A European Journal* 23 (2017): 9018–9021, https://doi.org/10.1002/chem.201701060.

16136829, 0, Downloaded from https://onlinelibrary.wiley.com/doi/10.1002/smll.75964 by Karlsruher Institut Fur Technologie, Wiley Online Library on [03/11/2026]. See the Terms and Conditions (https://onlinelibrary.wiley.com/terms-and-conditions) on Wiley Online Library for rules of use; OA articles are governed by the applicable Creative Commons License

51. M. Myahkostupov and F. N. Castellano, "Tetrahedral Rigid Core Antenna Chromophores Bearing Bay-Substituted Perylenediimides," *Tetrahedron* 71 (2015): 9519–9527, https://doi.org/10.1016/j.tet.2015.10.083.

52. H. Tohma, A. Maruyama, A. Maeda, et al., "Preparation and Reactivity of 1,3,5,7-Tetrakis[4-(diacetoxyiodo)phenyl]adamantane, a Recyclable Hypervalent Iodine(III) Reagent," *Angewandte Chemie International Edition* 43 (2004): 3595–3598, https://doi.org/10.1002/anie.200454234.

53. S. Gowrisankar, B. Bernhardt, J. Becker, and P. R. Schreiner, "Regioselective Synthesis of *meta* -Tetraaryl-Substituted Adamantane Derivatives and Evaluation of Their White Light Emission," *European Journal of Organic Chemistry* 2021 (2021): 6806–6810, https://doi.org/10.1002/ejoc.202101366.

54. A. Schwenger, W. Frey, and C. Richert, "Tetrakis(dimethoxyphenyl)Adamantane (TDA) and Its Inclusion Complexes in the Crystalline State: A Versatile Carrier for Small Molecules," *Chemistry – A European Journal* 21 (2015): 8781–8789, https://doi.org/10.1002/chem.201406568.

55. M. A. A. Ibrahim and E. M. Z. Telb, "σ-Hole and Lone-Pair Hole Interactions in Chalcogen-Containing Complexes: A Comparative Study," *ACS Omega* 5 (2020): 21631–21640, https://doi.org/10.1021/acsomega.0c02362.

56. H. Samuel, E. ETIM, and U. NwekeMaraizu, "Approaches for Special Characteristics of Chalcogen Bonding: A Mini Review," *Journal of Applied Organometallic Chemistry* 3 (2023): 199–212, https://doi.org/10.22034/jaoc.2023.405432.1089.

57. T. H. Lee and S. R. Elliott, "Hypervalency in Amorphous Chalcogenides," *Nature Communications* 13 (2022): 1458, https://doi.org/10.1038/s41467-022-29054-5.

58. P. Varadwaj, H. Marques, A. Varadwaj, and K. Yamashita, "Chalcogen···Chalcogen Bonding in Molybdenum Disulfide, Molybdenum Diselenide and Molybdenum Ditelluride Dimers as Prototypes for a Basic Understanding of the Local Interfacial Chemical Bonding Environment in 2D Layered Transition Metal Dichalcogenides," *Inorganics* 10 (2022): 11, https://doi.org/10.3390/inorganics10010011.

59. S. Alvarez, "A Cartography of the van der Waals Territories," *Dalton Transactions* 42 (2013): 8617–8636, https://doi.org/10.1039/c3dt50599e.

60. U. Herzog and G. Rheinwald, "Five- and Six-Membered Ring Group 14 Chalcogenides of the Types $(Me_2ME)_3$ (M=Si, Ge, Sn), $E(Si_2Me_4)_2E$, $Me_4Si_2(E)_2MRx$ (MRx = $C(CH_2)_5$, $SiMe_2$, $GeMe_2$, $SnMe_2$, $SnPh_2$, BPh) and $[Me_4Si_2(E)_2SiMe]_2$ (E = S, Se, Te)," *Journal of Organometallic Chemistry* 627 (2001): 23–36, https://doi.org/10.1016/S0022-328X(01)00707-0.

61. H. Lange, U. Herzog, U. Böhme, and G. Rheinwald, "Molecular Structures of Trimeric Diphenyltin Chalcogenides, $(Ph_2SnE)_3$, E = S, Se, Te," *Journal of Organometallic Chemistry* 660 (2002): 43–49, https://doi.org/10.1016/S0022-328X(02)01690-X.

62. K. Merzweiler and H. Kraus, "Notizen: Eine Neue Bicyclische Zinn-Selen-Verbindung. Synthese und Kristallstruktur von $[\{Cp(CO)_2Fe\}_3ClSn_3Se_4]$ /A New Bicyclic Tin Selenium Compound. Synthesis and Crystal Structure of $[\{Cp(CO)_2Fe\}_3ClSn_3Se_4]$," *Zeitschrift Für Naturforschung* 48 (1994): 621–626, https://doi.org/10.1515/znb-1993-0726.

63. K. Schwedtmann, A. Hepp, K. Schwedtmann, J. J. Weigand, and F. Lips, "Amido Silicon Chalcogenide Compounds with Unprecedented Cluster Cores and Low Oxidation State Silicon Atoms," *European Journal of Inorganic Chemistry* 2019 (2019): 4719–4726, https://doi.org/10.1002/ejic.201900954.

64. C. H. W. Jones, R. D. Sharma, and S. P. Taneja, "A Tellurium-125 and Tin-119 Mössbauer and Nuclear Magnetic Resonance Study of the Group IV Organotellurides," *Canadian Journal of Chemistry* 64 (1986): 980–986, https://doi.org/10.1139/v86-164.

65. R. W. Boyd, "The Nonlinear Optical Susceptibility," in *Nonlinear Optics*, 3rd ed., ed. R. W. Boyd (Academic Press, 2008), 1–67.

66. S. Grimme, J. Antony, S. Ehrlich, and H. Krieg, "A Consistent and Accurate Ab Initio Parametrization of Density Functional Dispersion Correction (DFT-D) for the 94 Elements H-Pu," *The Journal of Chemical Physics* 132 (2010): 154104, https://doi.org/10.1063/1.3382344.

67. S. Grimme, S. Ehrlich, and L. Goerigk, "Effect of the Damping Function in Dispersion Corrected Density Functional Theory," *Journal of Computational Chemistry* 32 (2011): 1456–1465, https://doi.org/10.1002/jcc.21759.

68. P. E. Blöchl, "Projector Augmented-Wave Method," *Physical Review B* 50 (1994): 17953–17979, https://doi.org/10.1103/PhysRevB.50.17953.

69. G. Kresse and D. Joubert, "From Ultrasoft Pseudopotentials to the Projector Augmented-wave Method," *Physical Review B* 59 (1999): 1758–1775, https://doi.org/10.1103/PhysRevB.59.1758.

70. C. Attaccalite and M. Grüning, "Nonlinear Optics from an Ab Initio Approach by Means of the Dynamical Berry Phase: Application to Second- and Third-Harmonic Generation in Semiconductors," *Physical Review B* 88 (2013): 235113, https://doi.org/10.1103/PhysRevB.88.235113.

71. F. Ziese, J. Wang, I. Rojas León, S. Dehnen, and S. Sanna, "Origin of the Nonlinear Optical Response in Organotetrel Molecules, (Hetero)Adamantane-Type Clusters with Organic Substituents, and Related Species," *The Journal of Physical Chemistry A* 128 (2024): 8360–8372, https://doi.org/10.1021/acs.jpca.4c03990.

72. G. M. Sheldrick, "SHELXT – Integrated Space-Group and Crystal-Structure Determination," *Acta Crystallographica Section A Foundations and Advances* 71 (2015): 3–8, https://doi.org/10.1107/S2053229614024218.

73. S. Grimme, C. Bannwarth, and P. Shushkov, "A Robust and Accurate Tight-Binding Quantum Chemical Method for Structures, Vibrational Frequencies, and Noncovalent Interactions of Large Molecular Systems Parametrized for All spd-Block Elements (Z = 1–86)," *Journal of Chemical Theory and Computation* 13 (2017): 1989–2009, https://doi.org/10.1021/acs.jctc.7b00118.

74. C. Bannwarth, E. Caldeweyher, S. Ehlert, et al., "Extended Tight-Binding Quantum Chemistry Methods," *WIREs Computational Molecular Science* 11 (2021): 1493, https://doi.org/10.1002/wcms.1493.

75. P. Pracht, E. Caldeweyher, S. Ehlert, and S. Grimme, "A Robust Non-Self-Consistent Tight-Binding Quantum Chemistry Method for Large Molecules," *ChemRxiv* (2019), https://doi.org/10.26434/chemrxiv.8326202.v1.

76. S. Grimme, "Exploration of Chemical Compound, Conformer, and Reaction Space with Meta-Dynamics Simulations Based on Tight-Binding Quantum Chemical Calculations," *Journal of Chemical Theory and Computation* 15 (2019): 2847–2862, https://doi.org/10.1021/acs.jctc.9b00143.

77. P. Pracht, F. Bohle, and S. Grimme, "Automated Exploration of the Low-Energy Chemical Space with Fast Quantum Chemical Methods," *Physical Chemistry Chemical Physics* 22 (2020): 7169–7192, https://doi.org/10.1039/c9cp06869d.

78. P. A. M. Dirac, "The Quantum Theory of the Electron," *Proceedings of the Royal Society of London Series A, Containing Papers of a Mathematical and Physical Character* 123 (1929): 714–733, https://doi.org/10.1039/c9cp06869d.

79. V. Fock, "Näherungsmethode zur Lösung des quantenmechanischen Mehrkörperproblems," *Zeitschrift für Physik* 61 (1930): 126–148, https://doi.org/10.1007/BF01340294.

80. J. C. Slater, "A Simplification of the Hartree-Fock Method," *Physical Review* 81 (1951): 385–390, https://doi.org/10.1103/PhysRev.81.385.

81. S. H. Vosko, L. Wilk, and M. Nusair, "Accurate Spin-dependent Electron Liquid Correlation Energies for Local Spin Density Calculations: A Critical Analysis," *Canadian Journal of Physics* 58 (1980): 1200–1211, https://doi.org/10.1139/p80-159.

82. A. D. Becke, "Density-Functional Exchange-Energy Approximation with Correct Asymptotic Behavior," *Physical Review A* 38 (1988): 3098–3100, https://doi.org/10.1103/PhysRevA.38.3098.

83. C. Lee, W. Yang, and R. G. Parr, "Development of the Colle-Salvetti Correlation-Energy Formula into a Functional of the Electron Density,"

16136829, 0, Downloaded from https://onlinelibrary.wiley.com/doi/10.1002/smll.75964 by Karlsruher Institut Fur Technologie, Wiley Online Library on [03/11/2026]. See the Terms and Conditions (https://onlinelibrary.wiley.com/terms-and-conditions) on Wiley Online Library for rules of use; OA articles are governed by the applicable Creative Commons License

Physical Review B 37 (1988): 785–789, https://doi.org/10.1103/PhysRevB.37.785.

84. A. D. Becke, "Density-functional Thermochemistry. I. The Effect of the Exchange-Only Gradient Correction," *The Journal of Chemical Physics* 96 (1992): 2155–2160, https://doi.org/10.1063/1.462066.

85. E. Caldeweyher, J.-M. Mewes, S. Ehlert, and S. Grimme, "Extension and Evaluation of the D4 London-Dispersion Model for Periodic Systems," *Physical Chemistry Chemical Physics* 22 (2020): 8499–8512, https://doi.org/10.1039/d0cp00502a.

86. T. H. Dunning, "Gaussian Basis Sets for Use in Correlated Molecular Calculations. I. The Atoms Boron through Neon and Hydrogen," *The Journal of Chemical Physics* 90 (1989): 1007–1023, https://doi.org/10.1063/1.456153.

87. R. A. Kendall, T. H. Dunning, and R. J. Harrison, "Electron Affinities of the First-Row Atoms Revisited. Systematic Basis Sets and Wave Functions," *The Journal of Chemical Physics* 96 (1992): 6796–6806, https://doi.org/10.1063/1.462569.

88. B. Metz, H. Stoll, and M. Dolg, "Small-Core Multiconfiguration-Dirac–Hartree–Fock-Adjusted Pseudopotentials for Post- d Main Group elements: Application to PbH and PbO," *The Journal of Chemical Physics* 113 (2000): 2563–2569, https://doi.org/10.1063/1.1305880.

89. K. A. Peterson, D. Figgen, E. Goll, H. Stoll, and M. Dolg, "Systematically Convergent Basis Sets with Relativistic Pseudopotentials. II. Small-Core Pseudopotentials and Correlation Consistent Basis Sets for the Post- d Group 16–18 Elements," *The Journal of Chemical Physics* 119 (2003): 11113–11123, https://doi.org/10.1063/1.1622924.

90. TURBOMOLE V7.5.1, a development of University of Karlsruhe and Forschungszentrum Karlsruhe GmbH, TURBOMOLE GmbH, since 2007 (TURBOMOLE GmbH, 2023), http://www.turbomole.com.

91. D. Sangalli, A. Ferretti, H. Miranda, et al., "Many-body Perturbation Theory Calculations Using the yambo Code," *Journal of Physics: Condensed Matter* 31 (2019): 325902, https://doi.org/10.1088/1361-648X/ab15d0.

92. J. P. Perdew, K. Burke, and M. Ernzerhof, "Generalized Gradient Approximation Made Simple," *Physical Review Letters* 77 (1996): 3865–3868, https://doi.org/10.1103/PhysRevLett.77.3865.

93. D. R. Hamann, "Optimized Norm-Conserving Vanderbilt Pseudopotentials," *Physical Review B* 88 (2013): 085117, https://doi.org/10.1103/PhysRevB.88.085117.

94. M. Schlipf and F. Gygi, "Optimization Algorithm for the Generation of ONCV Pseudopotentials," *Computer Physics Communications* 196 (2015): 36–44, https://doi.org/10.1016/j.cpc.2015.05.011.

95. P. Giannozzi, O. Andreussi, T. Brumme, et al., "Advanced Capabilities for Materials Modelling with Quantum ESPRESSO," *Journal of Physics: Condensed Matter* 29 (2017): 465901, https://doi.org/10.1088/1361-648X/aa8f79.

Supporting Information

Additional supporting information can be found online in the Supporting Information section.

Supporting File: smll75964-sup-0001-SuppMat.pdf.

16136829, 0, Downloaded from https://onlinelibrary.wiley.com/doi/10.1002/smll.75964 by Karlsruher Institut Fur Technologie, Wiley Online Library on [03/11/2026]. See the Terms and Conditions (https://onlinelibrary.wiley.com/terms-and-conditions) on Wiley Online Library for rules of use; OA articles are governed by the applicable Creative Commons License